Experimental Investigation of Pulsed, Eye-Safe, Solid-State Lasers in the Near Infrared

by

Serhat Tozburun

A Thesis Submitted to the

Graduate School of Engineering

in Partial Fulfillment of the Requirements for

the Degree of

Master of Science

in

Physics

Koç University

July 2007

Koc University

Graduate School of Sciences and Engineering

This is to certify that I have examined this copy of a master's thesis by

Serhat Tozburun

and have found that it is complete and satisfactory in all respects,
and that any and all revisions required by the final
examining committee have been made.

Committee Members:

_____

Alphan Sennaroğlu, Ph. D. (Advisor)

_____

Alper Kiraz, Ph.D.

_____

Alkan Kabakcıoğlu, Ph.D.

Date: _____

ii

ABSTRACT

In this work, three different pulsed, eye-safe, solid-state laser systems were experimentally constructed and characterized. The operation wavelengths of these sources were in the 1500-1600 nm range. The investigated systems include, 1064-nm-pumped potassium titanyl phosphate (KTP) optical parametric oscillator (OPO) at 1572 nm, flashlamp-pumped Er-glass laser at 1520 nm, and 1314-nm-pumped barium nitrate $(Ba(NO_3)_2)$ Raman laser at 1524 nm. A flashlamp driver was first built and used as the energy source in these experiments. In all cases, pulsed output was obtained by employing the technique of passive Q switching with different saturable absorbers. In the case of the KTP OPO, the Nd:YAG pump laser operating at 1064 nm was passively Q-switched by using a Cr^{4+}:YAG crystal. In the case of 1520-nm Er-glass and 1314-nm Nd:YAG lasers, cobalt-doped magnesium aluminates (Co^{2+}-doped $MgAl_2O_4$ or Co:MALO) was used for passive Q switching. For each case, both the pump as well as the eye-safe converting scheme was characterized in the long-pulse and short-pulse regimes. The best results were obtained with the Er-glass laser, where as high as 21-mJ pulses with duration of 40 ns were obtained at 1520 nm. In this case, the reflectivity of the output coupler was 75 %. The mechanism of passive Q switching was further modeled by using a rate equation approach. Passively Q-switched operation of the 1064-nm Nd:YAG, 1314-nm Nd:YAG, and 1520-nm Er-glass lasers was analyzed. Overall, very good agreement was obtained between the experimentally measured output pulse parameters and mode predictions.

ÖZET

Bu çalışmada, göze zararsız üç değişik katı-hal laser sistemi deneysel olarak incelenmiş ve karakterize edilmiştir. Bu laser kaynakları 1500-1600 nm dalgaboyu aralığında çalıştırılmıştır. Araştırılan sistemler içerisinde: 1064-nm-pompalı 1572-nm'de çalışan potasyum titanyum fosfat (KTP) optik parametrik osilatörü (OPO), 1520-nm'de çalışan flaşlambasıyla pompalanan erbiyum-cam (Er-glass) laseri ve 1314-nm-pompalı 1524-nm'de çalışan baryum nitrat ($Ba(NO_3)_2$) Raman laseri bulunmaktadır. İlk olarak flaşlamba sürücüsü yapılmış ve deneyler sırasında enerji kaynağı olarak kullanılmıştır. Tüm kurulan laserlerde, darbeli çıkış pasif Q-anahtar tekniği ile farklı doyabilen soğurucular kullanılarak elde edilmiştir. KTP OPO'ya pompa kaynağı olarak kullanılan Nd:YAG laserinin 1064-nm dalgaboyundaki darbe çıkışı, Cr^{4+}:YAG kristalinin doyabilen soğurucu şeklinde kullanılmasıyla elde edilmiştir. 1520-nm'de çıkışı olan erbiyum-cam ve 1314-nm'de çıkışı olan Nd:YAG laserlerinde, kobalt-katkılı magnezyum alüminat (Co^{2+}-katkılı $MgAl_2O_4$ yada Co:MALO) kristali pasif Q-anahtarlamalı çıkış darbesi üretebilmek için kullanılmıştır. En iyi sonuçlar erbiyum-cam laserinden elde edilmiştir. %75'lik yansıtmalı çıkış aynası kullanıldığında, enerjisi 21 mJ ve uzunluğu 40 ns'ye olan çıkış darbeleri ölçülmüştür. Nüfuz hız denklemleri (Rate Equations) kullanılarak pasif Q-anahtar mekanizması modellenmiştir. Pasif Q-anahtarlamalı 1064-nm ve 1314-nm dalgaboyunda çalıştırılan Nd:YAG laseri ile 1520-nm'de çıkışı olan Er-cam laseri teorik olarak analiz edilmiştir. Sonuç olarak, teorik olarak hesaplanan çıkış enerji değerleri ve darbe uzunlukları deneysel düzenekle elde edilenlerle ölçümlerle örtüştükleri gözlemlenmiştir.

ACKNOWLEDGEMENTS

I would gratefully acknowledge my best friend Ahmet Koray Erdamar for always being with me, his endless friendship and helping in all difficulties during my high-school, undergraduate and graduate years.

I wish to thank Selin Serim for her abundant confidence, deep love and continual support during my studies.

Finally, I am grateful to my family for their endless encouragement, patience, continuing support and love during my studies. It is to them, I wish to dedicate this thesis.

TABLE OF CONTENTS

LIST OF TABLES

LIST OF FIGURES

NOMENCLATURE

A	effective area
Al_c	effective volume
$A(z)$	area as a function of position
A_1	beam area at the entrance surface
A_2	beam area at the exit surface
c	speed of light
C	capacitance
C_{PT}	total capacitance in parallel combination
C_{ST}	total capacitance in series combination
C_T	total capacitance
E	output pulse energy
E_o	output energy
ESA	excited state absorption in saturable absorber
GSA	ground state absorption in saturable absorber
$(g_{th})_{average}$	average differential gain coefficient
g_o	Raman gain coefficient
g_R	steady-state stimulated Raman scattering gain
g_1	parameter
g_2	parameter
h	Plank constant
hv	photon energy
I	intensity of the radiation field in the medium
I_P	pump intensity
K	a constant

K_0	lamp-impedance parameter
L	fractional passive loss
L_{eff}	effective length
L_{ind}	inductance
l	coil length
l_c	effective length of the laser cavity
l_g	length of the gain medium
l_R	length of the Raman medium
l_{SA}	length of the saturable absorber
m	integer
n	population inversion density in the gain medium
n_f	final population inversion density
n_g	refractive index of gain medium
n_{KTP}	refractive index of KTP crystal
n_{ith}	initial threshold population inversion density
n_P	population inversion density where photon density reaches to max value
n_{SA}	population inversion density in the saturable absorber
n_{SAi}	initial density of the absorption state within the saturable absorber
n_{SA0}	total population density in the saturable absorber
n_{SA1}	population inversion density at the energy state 1
n_{SA2}	population inversion density at the energy state 2
n_{sa}	refractive index of saturable absorber
P	power
P_{max}	maximum power
P_{peak}	peak power
$P(t)$	power as a function of time (instantaneous power)

Q	optical quality factor
r	coil radius
r_{big}	semi major axis of elliptic spot
r_c	radius of curvature
r_{small}	semi minor axis of elliptic spot
R	reflectivity of the output coupler
R'	reflectivity of the first mirror
R_T	resistance
t	time
t_P	pulsewidth
t_r	time required to complete one roundtrip inside the resonator
T	one way transmission
T_i	optical transmissions of the ith internal element for one pass
T_o	small signal transmission
U	energy density
U_P	pulse energy per unity area
V	voltage
w_i	spot size
z	coordinate along the direction of propagation inside the absorber
α	a constant
α_T	net differential loss
α_L	differential loss coefficient
$\varnothing$	photon density
$\varnothing(t_m)$	average number of photon per unit volume at time t_m
ϕ_{max}	maximum photon density
γ	inversion reduction factor of gain medium

γ_{SA}	inversion reduction factor of saturable absorber
Γ	degree of the ESA relative to the GSA
λ	wavelength
ν	frequency of light
ν_{AS}	anti-stokes frequency
ν_P	pump frequency
ν_R	Raman shift
ν_S	stokes frequency
σ	stimulated emission cross-section
σ_{SA}	absorption cross-section
σ_{SESA}	excited state absorption cross-section
σ_{SGSA}	ground state absorption cross-section
τ	time
τ_f	fluorescence lifetime
υ	light velocity in the medium
ζ	non-saturable loss
$|f>$	final vibrational energy state
$|g>$	ground state
$|i>$	initial vibrational energy state
$|u>$	virtual upper state
$|1>$	first energy level
$|2>$	second energy level
$|3>$	third energy level
$|4>$	forth energy level

Chapter 1

INTRODUCTION

Nearly forty-seven years ago, T. H. Maiman demonstrated laser action successfully by using ruby crystal as the gain medium [1]. Since then, not only the term laser has been adopted into the daily speech but also many applications of lasers have entered our daily life. However, lasers operating in the visible and near-infrared spectral region ($0.4 - 1.4$ μm) may cause serious eye injuries [2]. Thus, protection against laser beam injury of the eyes becomes one of the important issues in the development of new lasers. However, if the laser operates in the 'eye-safe' region beyond 1.4 μm, we can use laser equipment more safely. This is because such a wavelength of light in this region of the spectrum is absorbed around the surface of the eyeball and it cannot reach the retina of the eyes [3], [4]. Thus, high peak power 'eye-safe' lasers attract great interest because of reducing the risk of eye damage.

Jelinkova et al. [4] presented the importance for applications of the lasers operating within the 'eye-safe' wavelength in their early demonstration of absorbed energy percentages in particular eye tissue segments; cornea, aqueous, lens, vitreous, and retina summarized in Table 1.1 below.

Laser	Wavelength (μ m)	Absorbed Energy (%)				
		Cornea	Aquesous	Lens	Vitreous	Retina
Alexandrite	0.75	20,0%	24,4%	10,0%	0,7%	44,8%
Nd:YAP	1.08	10,6%	9,7%	31,9%	2,2%	45,7%
Nd:YAP	1.34	26,4%	31,0%	28,5%	13,6%	0,5%
Er:Glass	1.54	86,7%	12,4%	0,9%	0,0%	0,0%
Er:YAP	1.66	53,6%	34,9%	10,6%	1,0%	0,0%
Tm:YAG	2.01	95,6%	4,3%	0,1%	0,0%	0,0%

Table 1.1: Absorbed energy in particular eye tissue segments for particular lasers.

There are many other application areas for lasers operating in the $1.5 - 1.6$ μm wavelength regime. For instance, they are used in the high precision ranging applications since such a wavelength of light has good propagation features in the atmosphere [5]. This is because, carbon dioxide and water vapor do not have strong absorption bands in this spectral range [6].

In this study, mainly two methods were used to obtain high-power laser radiation in the 'eye-safe' region. One of them is solid-state lasers with passively Q-switched erbium (Er)-doped Glass directly operating at $1.5 - 1.6$ μm. The other method is nonlinear optical conversion of radiation from Nd:YAG lasers. Optical parametric oscillation (OPO) in KTP crystal and stimulated Raman scattering (SRS) in barium nitrate ($Ba(NO_3)_2$) are used for non-linear optical conversion.

An early analysis of the Er:Glass laser was presented by Kalashnikov et al. [7]. They considered a flashlamp pumped Er:Glass laser operating at a 1 Hz repetition rate at 1.534 μm passively Q-switched by Co^{2+}-doped $MgAl_2O_4$ (MALO) crystal with 88% transmittance at the lasing wavelength. The Cr, Yb, Er – doped phosphate glass was used as a gain medium in a plane-concave cavity of 31 cm length. They made a theoretical model by solving rate equations describing Q-switched lasers. Excited-state absorption was included in their model. For 88% reflecting output coupler, 5 mJ output pulse energy was

obtained. They reported that the duration of the Q-switched pulses was around $70 - 75$ ns.

Later, other researchers employed the same gain medium and saturable absorber with 10% absorption at 1.5 μm. Bhardwaj et al. [8] further improved the Er:Glass laser. Similarly, they used plane-concave cavity. They could reduce the cavity length to 18 cm. For 80% output coupler, they obtained 5 mJ output pulse energy. The pulsewidth was measured to be 42.4 ns.

Zendzian et al. [5] presented an intra-cavity OPO in KTP crystal pumped at 1.064 μm from diode pumped passively Q-switched (Nd)–doped $Y_3Al_5O_{12}$ (YAG) laser. The Chromium (Cr) – doped $Y_3Al_5O_{12}$ (YAG) crystal was used as a passive Q-switch in the system. They achieved the highest pulse energy of 1.9 mJ with 2.9 ns duration for the saturable absorber of 52% transmission.

An early detailed analysis of Raman laser pumped by neodymium Nd:YAG laser operating at 1.338 μm by Chulkov et al. [6] presented the stimulated Raman scattering (SRS) in $Ba(NO_3)_2$ crystal. The Nd:YAG laser was Q-switched by using rotating roof prism. They report that, the output pulse energy of Nd:YAG laser was 250 mJ with 80% transmittance output coupler. By converting radiation coming from Nd:YAG laser, they measured pulses with energy of 120 mJ in the 1.556 μm region.

Murray et al. [9] reported an intra-cavity $Ba(NO_3)_2$ Raman laser pumped at 1.3 μm from flashlamp pumped Nd:YAG laser. Pulse energy of 0.25 J at the 1 Hz repetition rate was obtained at $1.535 - 1.556$ μm.

Chapter 2 gives details about our theoretical model based on the analytical and numerical solution of rate equations describing passively Q-switched laser systems. All steps are shown and variables are defined in the derivation of the differential equations.

Chapter 3 provides necessary background about pulse forming network (PFN) circuits used for driving the flashlamp. Moreover, details and required calculations are shown step by step in the construction of our particular laser driver design.

Theoretical background of optical parametric oscillation (OPO) and details of our KTP OPO system are given in chapter 4. Analysis of the pump source Nd:YAG laser, features of the components and positions in the resonator are described. Moreover, experimental results are presented and discussed.

In chapter 5, we start with a summary of the theoretical background about stimulated Raman scattering (SRS). Then, features of the barium nitrate Raman crystal are given. Moreover, details of the configuration of the flashlamp pumped Nd:YAG laser operating at $1.314 \ \mu$m. Processes in the intra-cavity and extra-cavity Raman lasers are described briefly. Finally, detailed results obtained from both configurations are given.

The last laser system operating at 'eye-safe' is the flashlamp-pumped Er:Glass laser Q-switched by Co:MALO. This is considered in chapter 6. The reason of using Cr:Yb:Er:Glass crystal as a gain medium is explained. After giving details about our particular Er:Glass laser design, the results that we obtained from both saturable absorber are discussed.

The thesis is concluded with a brief summary of the experiments and a discussion of the results.

Chapter 2

THEORETICAL ANALYSIS OF PASSIVELY
Q-SWITCHED LASERS

2.1   Introduction

In this chapter, we present the theoretical analysis of passively Q-switched flashlamp pumped solid state lasers. Q-switching is an operation mode of lasers for generating high peak power pulses. In this technique, the population inversion reaches high values without laser action occurring because of high loss in the cavity. While high loss prevents laser action, energy is stored in the active medium by optical pumping. After high population inversion has been achieved far above the threshold value for normal lasing, the loss in the cavity is suddenly reduced. At that moment, all available energy is emitted in the form of short pulse(s).

The standard tool for the theoretical analysis and optimization of the performance of passively Q-switched solid state lasers uses a set of coupled rate equations. For a passively O-switched laser, these basic rate equations are the time rate of change of the intra-cavity photon density, inversion density and ground state population inversion density of the saturable absorber. We will establish and solve the system of three coupled differential equations for the cases of pure absorption saturation and excited-state absorption. These are described in references [10] and [11].

2.2   Analysis of Passively Q-Switched Lasers Using the Degnan Method

Degnan's method which is described in reference [10] uses the plane-wave approximation and assumes a constant intensity across the beam cross-section. Furthermore, the role of excited-state absorption is neglected.

2.2.1 Laser Rate Equations

The photon density ϕ (t_m) is defined as the average number of photons per unit volume inside the resonator at time $t_m = mt_r$. The roundtrip time $t_r = 2l_c/c$ is the time required to complete one roundtrip inside the resonator. Here l_c is the effective length of the laser cavity and m is an integer. After an additional roundtrip, the photon density as time t_{m+1} is give by [12]

$$\phi(t_{m+1}) = \phi(t_m)\exp(2nl_g\sigma)\exp(-2n_{SA}l_{SA}\sigma_{SA})\exp(-2\alpha l_g)RR'\prod_i T_i^2 , \qquad (2.1)$$

where n is the instantaneous population inversion density in the gain medium at time t_m, n_{SA} is the instantaneous population inversion density in the ground state of the saturable absorber (SA) at time t_m, l_g and l_{SA} are the length of the gain medium and SA, respectively, σ and σ_{SA} are the stimulated emission and ground state absorption cross-sections of the gain medium and SA, respectively. α is the total differential loss coefficient in the laser rod, R is the reflectivity of the output coupler, R' is the reflectivity of the first mirror in the cavity and T_i is the optical transmission of the ith internal element for one pass.

By taking the natural logarithm of equation 2.1, we obtain

$$\Delta\ln\phi = \ln\phi(t_{m+1}) - \ln\phi(t_m) = 2nl_g\sigma - 2n_{SA}l_{SA}\sigma_{SA} - (\ln(\frac{1}{R}) + 2\alpha l_g + \ln(\frac{1}{R'\prod_i T_i^2})) . \qquad (2.2)$$

The first and the second terms describe the gain and the saturable loss, respectively. The last two terms are the passive losses in equation 2.2 and they can be combined into

$$L = 2\alpha l_g + \ln(\frac{1}{R'\prod_i T_i^2}), \tag{2.3}$$

where L is the total fractional passive loss in one roundtrip.

Equation 2.2 can be rewritten as

$$\Delta \ln \phi = 2nl_g\sigma - 2n_{SA}l_{SA}\sigma_{SA} - (\ln(\frac{1}{R}) + L). \tag{2.4}$$

We can expand the time rate of change of the photon density as follows

$$\frac{d\phi}{dt} = \phi \frac{d\ln\phi}{dt} = \phi \frac{\Delta \ln \phi}{\Delta t}. \tag{2.5}$$

The integer m is normalized to the roundtrip transit time of light in the resonator $\Delta m = \Delta t/t_r$. Thus, the time rate of change of the photon density is represented by

$$\frac{d\phi}{dt} = \frac{\phi}{t_r}(2nl_g\sigma - 2n_{SA}l_{SA}\sigma_{SA} - (\ln(\frac{1}{R}) + L)). \tag{2.6}$$

In the derivation of other rate equations for population inversion density of the gain medium changing with time, we start from the changes in the ion population density in the excited state at the beginning of the laser action, based on the assumption that nearly all of the laser ions are in the excited state. This gives

$$\frac{dn}{dt} = -\frac{n}{\tau_f} - \gamma\sigma(\frac{I}{h v})n, \tag{2.7}$$

where τ_f is the fluorescence lifetime, h is the Plank Constant, v is the frequency of light, the parameter γ is an "inversion reduction factor" [13] and I is the intensity of the radiation field in the medium.

This factor "inversion reduction" shows the net reduction in the population inversion after a photon is emitted [13]. In the four-level systems, the population inversion density is reduced by one for each emitted photon, which means that inversion reduction factor is equal to 1. This is because radiation takes place in the decay from second to first energy

state as seen in Figure 2.1 (a) and due to the rapid decay to the ground state the population of level 1 is negligible. On the other hand, this factor is equal to 2 for a three-level system. This demonstrates the fact that the population inversion is reduced by two for each emitted photon. The reason is that the atom decaying from the upper level automatically populates the lower laser level as seen in Figure 2.1 (b).
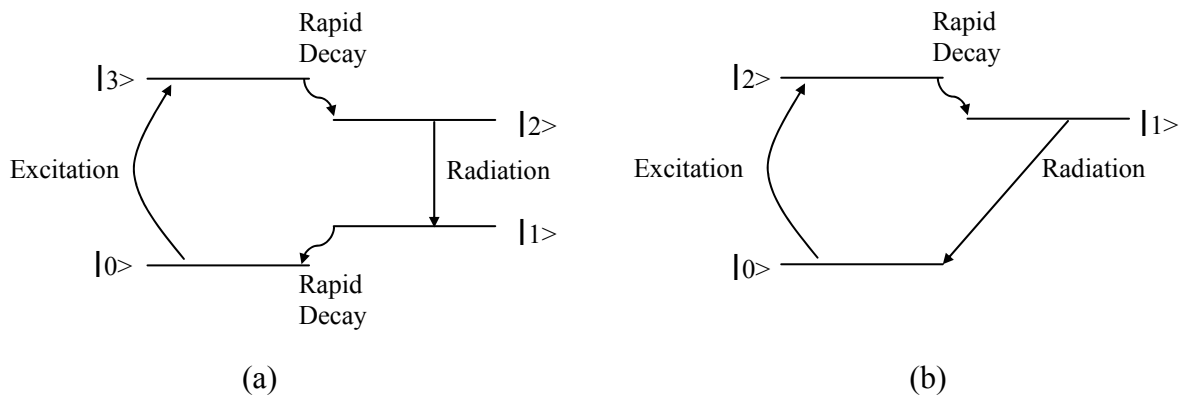
Figure 2.1: Energy level diagrams of (a) for +-level and (b) three level laser systems.

The term $I/h\nu$ in equation 2.7 shows the photon flux which is photon number ($\varnothing$) per cm^2 per second. The intensity of the radiation field in the gain medium is described by

$$I = U \times \upsilon, \tag{2.8}$$

where U is the energy density and υ is the light velocity in a medium. The energy density (U) is the product of the photon density with photon energy.

We neglect the refraction effects and assume that the light velocity in a medium is equal to speed of light in vacuum.

$$\upsilon \approx c. \tag{2.9}$$

When we neglect the first term in equation 2.7 and substitute equations 2.8 and 2.9 into 2.7, we have

$$\frac{dn}{dt} = -\sigma(\frac{chv\phi}{hv})n = -\gamma\sigma c\phi n .$$

(2.10)

The rate equation for the inversion density in the saturable absorber is obtained by using a similar approach as for the gain medium. The only difference is that the starting point is the absorption state of the SA. We assume that initially all ions in the SA are in the ground energy state.

$$\frac{dn_{SA}}{dt} = -\gamma_{SA}\sigma_{SA}c\phi n_{SA} .$$

(2.11)

The set of three coupled differential equations (rate equations) for the passively Q-switched solid-state lasers including the time rate of change of the photon density, time rate of change of the population inversion density in the gain medium and in the saturable absorber are summarized as follows:

$$\frac{d\phi}{dt} = \frac{\phi}{t_r}(2nl_g\sigma - 2n_{SA}l_{SA}\sigma_{SA} - (\ln(\frac{1}{R}) + L)),$$

$$\frac{dn}{dt} = -\gamma\sigma c\phi n,$$

$$\frac{dn_{SA}}{dt} = -\gamma_{SA}\sigma_{SA}c\phi n_{SA}.$$

(2.12)

2.2.2 Photon Density

In order to yield a relationship between the gain medium population inversion density (n) and the instantaneous population inversion density in the ground state of the SA (n_{SA}), equation 2.7 is divided by equation 2.11. The result is given by

$$\frac{dn}{dn_{SA}} = (\frac{\gamma\sigma}{\gamma_{SA}\sigma_{SA}})\frac{n}{n_{SA}} .$$

(2.13)

We introduce a new variable $\alpha = \gamma_{SA}\sigma_{SA}/\gamma\sigma$ and we arrange equation 2.13 as follows

$$\frac{dn}{n} = \frac{1}{\alpha}\frac{dn_{SA}}{n_{SA}}. \tag{2.14}$$

The differential equation 2.14 is solved when $n = n_{ith}$ and $n_{SA} = n_{SAi}$ at time t = 0 to estimate the relationship at all points in time.

$$\ln n_{ith} = \frac{1}{\alpha}\ln n_{SAi} + C,$$

$$C = \ln n_{ith} - \frac{1}{\alpha}\ln n_{SAi},$$

$$\ln n = \frac{1}{\alpha}\ln n_{SA} + C, \qquad\qquad . \tag{2.15}$$

$$\ln n = \frac{1}{\alpha}\ln n_{SA} + \ln n_{ith} - \frac{1}{\alpha}\ln n_{SAi},$$

$$\ln\frac{n}{n_{ith}} = \ln(\frac{n_{SA}}{n_{SAi}})^{1/\alpha}.$$

where n_{SAi} is the initial density of the absorbing state within the saturable absorber and n_{ith} is the initial threshold population inversion density just before Q-switching in the gain medium. By simplification of equation 2.15 the saturable absorber population inversion density (n_{SA}) is written

$$n_{SA} = n_{SAi}(\frac{n}{n_{ith}})^{\alpha}. \tag{2.16}$$

At starting point of the Q-switching, the saturable absorber population inversion density is equal to initial density $n_{SA} = n_{SAi}$.

Pulse generation begins at the point where population inversion density crosses the initial threshold population density. Thus, we set equation 2.6 equal to zero which means that gain equals to the loss within the resonator. The initial threshold inversion density (n_{ith}) is given by

$$n_{ith} = \frac{\sigma_{SA} l_{SA} n_{SAi}}{\sigma l_g} + \frac{\ln(\frac{1}{R}) + L}{2\sigma l_g} \,.$$ (2.17)

In order to determine the equation of the photon density (ϕ) first of all, equation 2.6 is divided by equation 2.7.

$$\frac{d\phi}{dn} = -\frac{1}{\gamma \sigma c n t_r} (2nl_g \sigma - 2n_{SA} l_{SA} \sigma_{SA} - (\ln(\frac{1}{R}) + L)),$$

$$= -\frac{l_g}{\gamma l_c} (1 - \frac{\sigma_{SA} n_{SA} l_{SA}}{\sigma n l_g} - \frac{(\ln(\frac{1}{R}) + L)}{2\sigma n l_g}).$$ (2.18)

After substituting expression of n_{SA} (2.16) into the differential equation 2.18, it becomes

$$\frac{d\phi}{dn} = -\frac{l_g}{\gamma l_c} (1 - \frac{\sigma_{SA} l_{SA}}{\sigma l_g} \frac{n_{SAi}}{n_i} (\frac{n}{n_i})^{\alpha-1} - \frac{(\ln(\frac{1}{R}) + L)}{2\sigma n l_g}) \,.$$ (2.19)

Then, resultant differential equation can be integrated over population inversion density from n to the n_{ith} to yield

$$\phi(n) = \int_{n_{thi}}^{n} -\frac{l_g}{\gamma l_c}(1 - \frac{\sigma_{SA} l_{SA}}{\sigma l_g} \frac{n_{SAi}}{n_{ith}}(\frac{n}{n_{ith}})^{\alpha-1} - \frac{(\ln(\frac{1}{R}) + L)}{2\sigma n l_g})dn,$$

$$= \int_{n_{ith}}^{n} -\frac{l_g}{\gamma l_c}(1 - \frac{l_{SA}\gamma}{l_g\gamma_{SA}}\alpha \frac{n_{SAi}}{n_{ith}}(\frac{n}{n_{ith}})^{\alpha-1} - \frac{(\ln(\frac{1}{R}) + L)}{2\sigma n l_g})dn,$$

$$= \frac{l_g}{\gamma l_c}(n_{ith} - n - \frac{l_{SA}\gamma}{l_g\gamma_{SA}} \frac{n_{SAi}}{n_{ith}}(\frac{n_{ith}^{\alpha}}{n_{ith}^{\alpha-1}} - \frac{n^{\alpha}}{n_{ith}^{\alpha-1}}) - \frac{(\ln(\frac{1}{R}) + L)}{2\sigma l_g}\ln(\frac{n_{ith}}{n})), \qquad (2.20)$$

$$= \frac{l_g}{\gamma l_c}(n_{ith} - n - \frac{l_{SA}\gamma}{l_g\gamma_{SA}} \frac{n_{SAi}}{n_{ith}} n_{ith}(1 - \frac{n^{\alpha}}{n_{ith}^{\alpha}}) - \frac{(\ln(\frac{1}{R}) + L)}{2\sigma l_g}\ln(\frac{n_{ith}}{n})),$$

$$= \frac{l_g}{\gamma l_c}(n_{ith} - n - \frac{l_{SA}\gamma}{l_g\gamma_{SA}} n_{SAi}(1 - (\frac{n}{n_{ith}})^{\alpha}) - \frac{(\ln(\frac{1}{R}) + L)}{2\sigma l_g}\ln(\frac{n_{ith}}{n})).$$

2.2.3 Output Energy

In order to determine the laser output pulse energy, first of all the instantaneous peak power should be obtained. By using equation 2.6, the instantaneous peak power coupled out from the cavity is given by [10, 12]

$$P(t) = -h\nu A l_c \frac{d\phi}{dt}\bigg|_R ,$$

$$\frac{d\phi}{dt}\bigg|_R = -\frac{\phi}{t_r}\ln(\frac{1}{R}), \qquad (2.21)$$

$$P(t) = h\nu A l_c \frac{\phi}{t_r}\ln(\frac{1}{R}),$$

where Al_c is the effective volume occupied by the photons and $h\nu$ is the photon energy. The minus sign shows that the instantaneous peak power is related to the reduction of the

photon number in the resonator. The laser output energy is directly equal to the integral of the peak power over time from zero to infinity

$$E = \int_0^\infty P(t)dt = hvAl_c \ln(\frac{1}{R})\frac{1}{t_r}\int_0^\infty \phi(t)dt \ . \tag{2.22}$$

In order to integrate equation 2.22, we need to change the variable of the integration from time to population inversion density and the new integral is from initial to final population inversion density. By using the equation 2.7, the integral is given by

$$dt = -\frac{1}{\gamma \sigma c \phi}\frac{dn}{n} ,$$

$$E = -\frac{hvAl_c}{\gamma \sigma c \phi t_r}\ln(\frac{1}{R})\int_{n_{ith}}^{n_f}\frac{dn}{n} = -\frac{hvAl_c}{\gamma \sigma c \phi \frac{2l_c}{c}}\ln(\frac{1}{R})\int_{n_i}^{n_f}\frac{dn}{n} . \tag{2.23}$$

The expression of the output energy is obtained

$$E = \frac{hvA}{2\gamma \sigma}\ln(\frac{1}{R})\ln(\frac{n_{ith}}{n_f}) \ . \tag{2.24}$$

The final inversion density (n_f) should be determined in calculating output pulse energy by using equation 2.24. In order to do that the photon density as a function of population inversion density is set equal to zero yielding transcendental equation

$$n_f = n_{ith} - \frac{\ln(\frac{1}{R}) + L}{2\sigma l_g}\ln(\frac{n_{ith}}{n_f}) - \frac{l_{SA}\gamma}{l_g\gamma_{SA}}n_{SAi}(1-(\frac{n_f}{n_{ith}})^\alpha) \ . \tag{2.25}$$

The last term of equation 2.25 shows the effect of the saturable absorber. This equation must be solved numerically because of the transcendental nature of it.

2.2.4 Pulsewidth Calculations

It is assumed that the shape of the output pulse can be thought as an asymmetric triangle. The height is maximum peak power (P_{max}), baseline width is time (t_b) and the area of the

triangle is the output pulse energy (E). The pulsewidth (t_p) is the ratio of the output pulse energy to the maximum peak power as the following expression

$$t_p = \frac{t_b}{2} = \frac{E}{P_{max}}. \tag{2.26}$$

We need to determine the maximum photon density (ϕ_{max}) to estimate maximum peak power. The photon density in the resonator reaches its maximum value when the population inversion density becomes equal to its threshold value. By using equation 2.20, the maximum photon density is given by

$$\phi_{max} = \frac{l_g}{\gamma l_c}(n_{ith} - n_p - \frac{l_{SA}\gamma}{l_g\gamma_{SA}} n_{SAi}(1 - \frac{n_p}{n_{ith}})^\alpha - \frac{(\ln(\frac{1}{R}) + L)}{2\sigma l_g}\ln(\frac{n_{ith}}{n_p})). \tag{2.27}$$

By using equation 2.21, the maximum peak power can be written as follows:

$$P_{max} = h\nu A l_c \frac{\phi_{max}}{t_r}\ln(\frac{1}{R}). \tag{2.28}$$

The population inversion density (n_p) can be obtained by setting equation 2.19 equal to zero ($d\phi/dn = 0$). Thus, we can obtain the expression for the threshold inversion density where the power has reaches maximum value

$$1 - \frac{\sigma_{SA}l_{SA}}{\sigma l_g} n_{SAi}(\frac{n_p}{n_{ith}})^\alpha (\frac{n_{ith}}{n_p}) - \frac{(\ln(\frac{1}{R}) + L)}{2\sigma n_p l_g} = 0,$$

$$\frac{n_{ith}}{n_p}(\frac{n_p}{n_{ith}} - \frac{\sigma_{SA}l_{SA}}{\sigma l_g} n_{SAi}(\frac{n_p}{n_{ith}})^\alpha - \frac{(\ln(\frac{1}{R}) + L)}{2\sigma n_{ith} l_g}) = 0, \tag{2.29}$$

$$\frac{n_p}{n_{ith}} = \frac{\sigma_{SA}l_{SA}}{\sigma l_g} n_{SAi}(\frac{n_p}{n_{ith}})^\alpha + \frac{(\ln(\frac{1}{R}) + L)}{2\sigma n_i l_g}.$$

After substituting equation 2.24 and 2.28 into equation 2.26, The pulsewidth (FWHM) is given by

$$t_p = \frac{t_r \ln(\frac{n_{ith}}{n_f})}{2\gamma\sigma l_c \phi_{nax}} .$$ (2.30)

By using equation 2.24, natural logarithm of the ratio of the initial population inversion density to the final population inversion density can be determined:

$$\ln(\frac{n_{ith}}{n_f}) = \frac{2\sigma l_g n_{ith}}{\ln(\frac{1}{R}) + L}\{1 - \frac{n_f}{n_{ith}} - \frac{l_{SA}\gamma}{l_g \gamma_{SA}} n_{SAi}(1 - (\frac{n_f}{n_{ith}})^\alpha)\} .$$ (2.31)

The final step of determining the expression of the pulse duration is substituting the expression of the maximum photon density (equations 2.27 and 2.31) into the last equation of the pulsewidth (2.30). The resultant pulse duration is now given by

$$t_p = \frac{t_r}{\ln(\frac{1}{R}) + L}\{\frac{1 - \frac{n_f}{n_{ith}} - \frac{l_{SA}\gamma}{l_g \gamma_{SA}} \frac{n_{SAi}}{n_{ith}}(1 - (\frac{n_f}{n_{ith}})^\alpha)}{1 - \frac{n_p}{n_{ith}} + \frac{\ln(\frac{1}{R}) + L}{2\sigma l_g n_{ith}}\ln(\frac{n_p}{n_{ith}}) - \frac{l_{SA}\gamma}{l_g \gamma_{SA}} \frac{n_{SAi}}{n_{ith}}(1 - (\frac{n_p}{n_{ith}})^\alpha)}\} .$$ (2.32)

2.3   Analysis of Passively Q-Switched Lasers Using the Zhang Method

The Zhang method described in reference [11] uses plane-wave approximation similar to the previous method. In typical passively Q-switched lasers, excited-state absorption also plays a role and provides an additional loss mechanism. In this section, we include the effects of ESA in the rate equation model of passive Q-switching.

2.3.1   Laser Rate Equations

This method is developed for four-level solid-state saturable absorber and a general four-level model is shown in Figure 2.2. We start by writing the photon transport equation [14]:

$$\frac{\partial I}{\partial z} + \frac{1}{c}\frac{\partial I}{\partial t} = -n_{SA1}\sigma_{SGSA}I - n_{SA2}\sigma_{SESA}I - I\zeta,\tag{2.33}$$

where c is the speed of light, n_{SA1} and n_{SA2} are the population inversion densities in states 1 and 2, respectively, σ_{SGSA} and σ_{SESA} are the ground state and excited state absorption cross sections, I is the light intensity, ζ is the non-saturable losses, and z is the coordinate along the direction of propagation inside the SA. On the right hand side, the second term is accounts for the effect of ESA. Since only states 1 and 2 are effectively populated, the relation between the population densities becomes

$$n_{SA1} + n_{SA2} \approx n_{SA0}.\tag{2.34}$$

After substituting equation 2.34 into the (2.33), we obtain

$$\frac{\partial I}{\partial z} + \frac{1}{c}\frac{\partial I}{\partial t} = -n_{SA1}\sigma_{SGSA}I - (n_{SAo} - n_{SA1})\sigma_{SESA}I - I\zeta,$$
$$\frac{\partial I}{\partial z} + \frac{1}{c}\frac{\partial I}{\partial t} = -n_{SA1}I(\sigma_{SGSA} - \sigma_{SESA}) - n_{SA0}\sigma_{SESA}I - I\zeta.\tag{2.35}$$

The time rate of change of population in state 1 is

$$\frac{\partial n_{SA1}}{\partial t} = -A\sigma_{SGSA}n_{SA1} = \frac{\sigma_{SGSA}I}{h\nu}n_{SA1},$$
$$n_{SA1} = -\frac{h\nu}{\sigma_{SGSA}I}\frac{\partial n_{SA1}}{\partial t}.\tag{2.36}$$
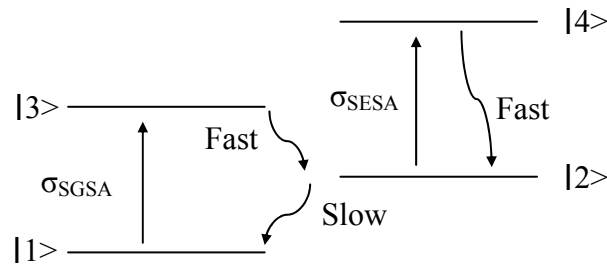
Figure 2.2: Energy levels diagram of a solid –state SA with GSA and ESA.

By substituting equation 2.36 into 2.35, we obtain

$$\frac{\partial I}{\partial z} + \frac{1}{c}\frac{\partial I}{\partial t} = \frac{h\nu}{\sigma_{SGSA}}(\sigma_{SGSA} - \sigma_{SESA})\frac{\partial n_{SA1}}{\partial t} - n_{SA0}\sigma_{SESA}I - I\zeta. \qquad (2.37)$$

We integrate equation 2.37 over time from minus infinity ($t = -\infty$) to a definite time ($t = \tau$). These time window covers the entire duration of the light pulse.

$$\int_{-\infty}^{t}\frac{\partial I}{\partial z}dt + \frac{1}{c}\int_{-\infty}^{t}\frac{\partial I}{\partial t}dt = \frac{h\nu}{\sigma_{SGSA}}(\sigma_{SGSA} - \sigma_{SESA})\int_{-\infty}^{t}\frac{\partial n_{SA1}}{\partial t}dt - n_{SA0}\sigma_{SESA}\int_{-\infty}^{t}Idt - \zeta\int_{-\infty}^{t}Idt. \qquad (2.38)$$

In this integration, we have used two well known facts. One of them is that

$$\int_{-\infty}^{t}Idt = U_P, \qquad (2.39)$$

where U_p is the pulse energy per unit area. The other fact is that

$$\frac{1}{c}\int_{-\infty}^{t}\frac{\partial I}{\partial t}dt = \frac{1}{c}(I(\tau) - I(-\infty)) = 0. \qquad (2.40)$$

Substituting equations 2.39 and 2.40 into the 2.38 and integrating the result, we obtain

$$\frac{\partial U_P}{\partial z} = \frac{h\nu}{\sigma_{SGSA}}(\sigma_{SGSA} - \sigma_{SESA})(n_{SA1}(\tau) - n_{SA0}) - n_{SA0}\sigma_{SESA}U_P - U_P\zeta. \qquad (2.41)$$

We can find out $n_{SA1}(\tau)$ by integrating equation 2.36. This gives

$$\int_{n_o}^{n_1(t)}\frac{dn_{SA1}}{n_{SA1}} = -\int_{-\infty}^{t}\frac{\sigma_{SGSA}I}{h\nu}dt. \qquad (2.42)$$

The result is

$$\ln(\frac{n_{SA1}(\tau)}{n_{SA0}}) = -\frac{\sigma_{SGSA}}{h\nu}U_P, \qquad (2.43)$$

or equivalently,

$$n_{SA1}(\tau) = n_{SAo}Exp(-\frac{\sigma_{SGSA}U_P}{h\nu}). \qquad (2.44)$$

Substituting equation 2.44 into equation 2.41, we have

$$\frac{\partial U_P}{\partial z} = \frac{hv}{\sigma_{SGSA}}(\sigma_{SGSA} - \sigma_{SESA})(n_{SA0}Exp(-\frac{\sigma_{SGSA}U_P}{hv}) - n_{SA0}) - n_{SA0}\sigma_{SESA}U_P - U_P\zeta. \qquad (2.45)$$

After some algebra, the resultant equation becomes

$$\frac{\partial U_P}{\partial z} = -hvn_{SAo}(1 - \frac{\sigma_{SESA}}{\sigma_{SGSA}})(1 - Exp(-\frac{\sigma_{SGSA}U_P}{hv})) - n_{SAo}\sigma_{SESA}U_P - U_P\zeta. \qquad (2.46)$$

Equation 2.46 does not include the non-saturable absorption within the SA. n_{SA0} is the total population density participating in the pulse generation.

We investigate two different limits of pulse energy. In the small energy limit,

$$Exp(-\sigma_{SGSA}U_P/hv) \approx 1 - \sigma_{SGSA}U_P/hv. \qquad (2.47)$$

In this case, the transmission of the SA is called small-signal transmission (T_o). When energy is large enough,

$$Exp(-\sigma_{SGSA}U_P/hv) \approx 0. \qquad (2.48)$$

When this situation is valid, transmission of the SA is called saturated transmission (T_S). Substituting results coming out from these two extreme cases equation 2.46 becomes

$$\frac{\partial U_P}{\partial z} = -n_{SA0}\sigma_{SGSA}U_P - U_P\zeta, \qquad (2.49)$$

and

$$\frac{\partial U_P}{\partial z} = -hvn_{SA0}(1 - \frac{\sigma_{SESA}}{\sigma_{SGSA}}) - n_{SA0}\sigma_{SESA}U_P - U_P\zeta. \qquad (2.50)$$

When we integrate equations 2.49 and 2.50 by neglecting the non-saturable terms and the first term in equation 2.50, we obtain the two respective expressions

$$2\sigma_{SGSA}n_{SA0}l_{SA} = \ln(\frac{1}{T_o^2}), \qquad (2.51)$$

and

$$2\sigma_{SESA} n_{SA0} l_{SA} = \ln(\frac{1}{T_S^2}),$$ (2.52)

where l_{SA} is the thickness of the SA as in the previous rate equation derivation.

Dividing equation 2.51 by 2.52, we have

$$\Gamma = \frac{\sigma_{SESA}}{\sigma_{SGSA}},$$ (2.53)

where the new parameter Γ indicates the degree of the ESA relative to the GSA.

By following similar derivation steps [10], three coupled rate equations are derived to account for the role of ESA and GSA in the SA [11]. The following modified differential equations describe passive Q-switching with a four-level saturable absorber:

$$\frac{d\phi}{dt} = \frac{\phi}{t_r}(2nl_g\sigma - 2n_{SA1} l_{SA}\sigma_{SGSA} - 2\sigma_{SESA} l_{SA}(n_{SA0} - n_{SA1}) - (\ln(\frac{1}{R}) + L)).$$ (2.54)

$$\frac{dn}{dt} = -\gamma\sigma c\phi n.$$ (2.55)

$$\frac{dn_{SA1}}{dt} = -\gamma_{SA}\sigma_{SGSA} c\phi n_{SA1}.$$ (2.56)

Above, l_g is the length of the gain medium, R is the reflectivity of the output coupler at lasing wavelength, σ is the stimulated emission cross section, L is the dissipative optical loss, ϕ is the photon density within the cavity, γ and γ_{SA} are the inversion reduction factors in the gain medium and SA, respectively.

2.3.2   Photon Density

In order to derive expression of the photon density as a function of instantaneous population inversion density (n), we need to divide equation 2.54 by 2.55. The differential equation is

$$\frac{d\phi}{dn} = \frac{-1}{t_r\gamma\sigma cn}(2nl_g\sigma - 2n_{SA1} l_{SA}\sigma_{SGSA} - 2\sigma_{SESA} l_{SA}(n_{SA0} - n_{SA1}) - (\ln(\frac{1}{R}) + L)).$$ (2.57)

The parameter n_{SA1} (the population inversion density in state 1) should be estimated. When we divide equation 2.55 by 2.56, we obtain

$$\frac{dn}{dn_{SA1}} = \frac{\gamma\sigma}{\gamma_{SA}\sigma_{SGSA}} .$$ (2.58)

We can use the parameter $\alpha = \dfrac{\gamma_{SA}\sigma_{SGSA}}{\gamma\sigma}$ similar to Degnan's method. Substituting the parameter α into equation 2.58 and integrating from $n = n_i$ to $n_{SA1} = n_{SA0}$, we obtain

$$n_{SA1} = n_{SA0}(\frac{n}{n_{ith}})^\alpha .$$ (2.59)

where n_{ith} is the initial population inversion density at the starting of Q-switching. After some algebra, differential equation 2.57 can be modified

$$\frac{d\phi}{dn} = \frac{-l_g}{\gamma l_c}(1 - \frac{n_{SA1}l_{SA}\sigma_{SGSA}}{nl_g\sigma} - \frac{l_{SA}\sigma_{SESA}(n_{SA0} - n_{SA1})}{nl_g\sigma} - \frac{\ln(\frac{1}{R}) + L}{2nl_g\sigma}) .$$ (2.60)

Substituting equation 2.53 and 2.58 into the result yields

$$\frac{d\phi}{dn} = \frac{-l_g}{\gamma l_c}(1 - \frac{n_{SA0}l_{SA}\sigma_{SGSA}}{nl_g\sigma}(\frac{n}{n_{ith}})^\alpha - \frac{\Gamma n_{SA0}l_{SA}\sigma_{SGSA}(1 - (\frac{n}{n_{ith}})^\alpha)}{nl_g\sigma} - \frac{\ln(\frac{1}{R}) + L}{2nl_g\sigma})$$

$$\frac{d\phi}{dn} = \frac{-l_g}{\gamma l_c}(1 - \frac{n_{SA0}l_{SA}\sigma_{SGSA}(1 - \Gamma)}{nl_g\sigma}(\frac{n}{n_{ith}})^\alpha - \frac{(\ln(\frac{1}{R}) + L) + \Gamma 2n_{SA0}l_{SA}\sigma_{SGSA}}{2nl_g\sigma})$$ (2.61)

The resultant differential equation is integrated over population inversion density form initial to definite inversion density value. This gives

$$\phi(n) = \frac{-l_g}{\mathcal{A}_c} \{ \int_{nith}^{n} dn - \int_{nith}^{n} (\frac{n_{SA0} l_{SA} \sigma_{SGSA}(1-\Gamma)}{l_g \sigma}) \frac{1}{n} (\frac{n}{n_{ith}})^{\alpha} - \frac{(\ln(\frac{1}{R})+L)+\Gamma 2 n_{SA0} l_{SA} \sigma_{SGSA}}{2 l_g \sigma n}) dn \}$$

$$= \frac{-l_g}{\mathcal{A}_c} \{ n - n_{ith} - \frac{(\ln(\frac{1}{R})+L)+\Gamma 2 n_{SA0} l_{SA} \sigma_{SGSA}}{2 l_g \sigma} \ln(\frac{n}{n_{ith}}) - \frac{n_{SA0} l_{SA} \sigma_{SGSA}(1-\Gamma)}{l_g \sigma n_{ith}} \int_{ni}^{n} (\frac{n}{n_{ith}})^{\alpha-1} dn \}$$

$$= \frac{-l_g}{\mathcal{A}_c} \{ n - n_{ith} - \frac{(\ln(\frac{1}{R})+L)+\Gamma 2 n_{SA0} l_{SA} \sigma_{SGSA}}{2 l_g \sigma} \ln(\frac{n}{n_{ith}}) - \frac{n_{SA0} l_{SA} \sigma_{SGSA}(1-\Gamma)}{l_g \sigma n_{ith}} \frac{(n^{\alpha} - n_{ith}^{\alpha})}{n_{ith}^{\alpha-1} \alpha} \}$$

$$= \frac{l_g}{\mathcal{A}_c} \{ n_{ith} - n - \frac{(\ln(\frac{1}{R})+L)+\Gamma 2 n_{SA0} l_{SA} \sigma_{SGSA}}{2 l_g \sigma} \ln(\frac{n_{ith}}{n}) - \frac{n_{SA0} l_{SA} \sigma_{SGSA}(1-\Gamma)}{l_g \sigma} \frac{1}{\alpha} (1-(\frac{n}{n_{ith}})^{\alpha}) \}$$

. (2.62)

2.3.3   Output Energy and Pulsewidth

The output energy (E_o), peak power (P) and pulsewidth (t_p) can be obtained in the same way similar to ref. [6], as we discussed in the previous section:

$$E_o = \frac{h\nu A}{2\gamma\sigma} \ln(\frac{1}{R}) \ln(\frac{n_{ith}}{n_f}) . \tag{2.63}$$

$$P_{nax} = h\nu A l_c \frac{\phi_{nax}}{t_r} \ln(\frac{1}{R}) . \tag{2.64}$$

$$t_p = \frac{E}{P_{\max}} . \tag{2.65}$$

Above A is the effective area of the beam in the laser medium, n_f is the final population inversion density and l_c is the length of the cavity.

At the beginning of Q-switched laser pulse generation, the radiation of the cavity generates small number photon in the laser resonator. When the maximum instantaneous power is reached, the photon density rises to its maximum value.

The maximum photon density can be written as follows:

$$\phi_{max}(n_p) = \frac{l_g}{\gamma l_c}\{n_{ith} - n_p - \frac{K}{2l_g\sigma}\ln(\frac{n_{ith}}{n_p}) - \frac{n_{SA0}l_{SA}\sigma_{SGSA}(1-\Gamma)}{l_g\sigma\alpha}(1-(\frac{n_p}{n_{ith}})^\alpha)\}. \tag{2.66}$$

Above n_p is the population inversion density at the point of maximum power and

$K = (\ln(\frac{1}{R}) + L) + \Gamma 2n_{SA0}l_{SA}\sigma_{SGSA}$ is a new parameter for simplification of the derivation.

By setting equation 2.54 equal to zero and using the facts that $n_{SA1}(t = 0) = n_{SA0}$ and

$n_{SA2}(t = 0) = 0$, we can obtain the initial threshold inversion density (n_{ith}) where laser pulse

generation begins.

$$n_{ith} = \frac{\ln(\frac{1}{R}) + L + 2\sigma_{SGSA}n_{SA0}l_{SA}}{2\sigma l_g}. \tag{2.67}$$

In order to calculate output pulse energy, we need to estimate the final inversion density

(n_f). At the end of the Q-switched pulse, photon density within the cavity becomes zero. By

setting equation 2.62 equal to zero, we can obtain the expression for the final population

inversion density n_f:

$$n_f = n_{ith} - \frac{K}{2l_g\sigma}\ln(\frac{n_{ith}}{n_f}) - \frac{n_{SA0}l_{SA}\sigma_{SGSA}(1-\Gamma)}{l_g\sigma}\frac{1}{\alpha}(1-(\frac{n_f}{n_{ith}})^\alpha). \tag{2.68}$$

In the peak power calculation, the maximum photon density should be estimated. As

seen in equation 2.66, n_p is the unknown parameter. When the photon density reaches its

maximum value, it does not change according to the inversion density anymore at that

moment. Thus, we can say that $d\phi/dn = 0$. By setting equation 2.61 equal to zero, we can

obtain an expression for n_p.

$$\frac{n_p}{n_{ith}} = \frac{n_{SA0}l_{SA}\sigma_{SGSA}(1-\Gamma)}{n_{ith}l_g\sigma}(\frac{n}{n_{ith}})^\alpha - \frac{(\ln(\frac{1}{R}) + L) + \Gamma 2n_{SA0}l_{SA}\sigma_{SGSA}}{2n_{ith}l_g\sigma}. \tag{2.69}$$

Now, the output energy E_0, peak power P, and pulsewidth t_P can be obtained by estimating inversion density ratios between n_f to n_{ith} and n_p to n_{ith} with equations 2.68 and 2.69.

2.4   Discussion

In the optimization of the performance of Q-switched lasers, three coupled rate equations generalized in the previous sections are used as a standard tool and they are solved numerically. The key parameters are the reflectivity of the output coupler and the initial transmission of the saturable absorber. These can be changed to maximize the output pulse energy and/or minimize the pulsewidth.

Our main goal is the optimization of the passively q-switched laser performance for fixed cavity length and the total fractional passive losses. The graphs of the output pulse energy as a function of reflectivity of output coupler and initial transmission of the saturable absorber (*To*) are plotted in Figures 2.3 and 2.4, respectively. Fixed parameters used in modeling graphs are listed in Table 2.1 below [13, 15-21].

laser	Nd:YAG
laser wavelength (nm)	1064
length of the gain medium (cm)	32.2
emission cross-section (cm^2)	6.5×10^{-19}
effective area (cm^2)	0.312
saturable Absorber (SA)	Cr^{4+}:YAG
length of the SA (cm)	0.3
GSA (cm^2)	$10\text{-}50 \times 10^{-19}$
initial transmission	0.5
length of the cavity (cm)	32.2
loss (L)	0.03

Table 2.1: Gain medium, saturable absorber and cavity parameters used in the theoretical modeling.
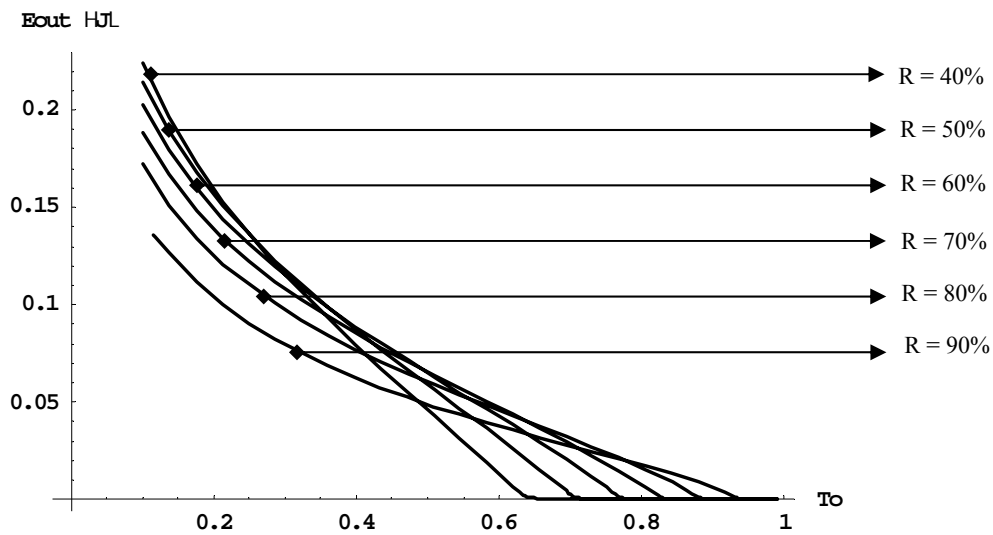
Figure 2.3: Calculated variation of the output pulse energy (Eout) as a function of the initial transmission of the saturable absorber (To) for different values of output coupler reflectivity (R).
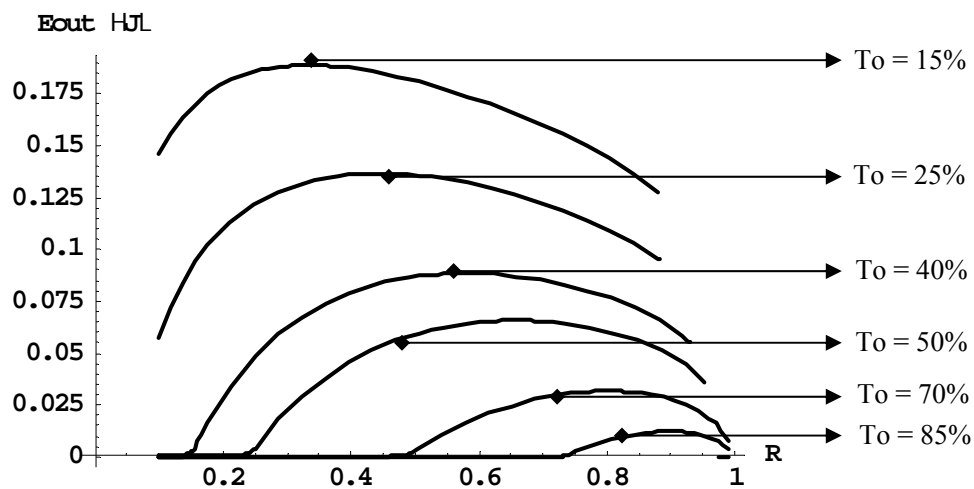
Figure 2.4: Calculated variation of the output pulse energy (Eout) as a function of output coupler reflectivity (R) for different values of the initial transmission of the saturable absorber (To).

From Figure 2.3, the output pulse energy (Eout) decreases monotonically as a function of the initial transmission of the saturable absorber for a given reflectivity. Using low values of To and R are expected to yield large output pulse energy. On the other hand, this increases the threshold pump energy necessary for obtaining lasing.

Looking at the Figure 2.4, there is an optimum reflectivity where the output pulse energy becomes maximum for a given value of small-signal transmission To. The optimum value of R approaches unity as To decreases.

Chapter 3

DESIGN AND CONSTRUCTION OF THE FLASHLAMP DRIVER

3.1   Overview

Flashlamps used for exciting solid-state lasers are essentially designed as long arc devices so that the plasma fills the tube. The filled gas inside the lamp is most often xenon because it yields a higher radiation output for a given electrical input energy than that of other gases [13]. Moreover, it converts 40 to 60% of the electrical input energy into radiation in the 0.2 -1.0 μm region [13]. The absorption of Nd:YAG is in the range of 0.3 to 0.9 μm [22]. Thus, flashlamps filled with xenon are widely used for pumping pulsed solid-state lasers such as Nd:YAG. Flashlamps are pulsed sources of light. They are operated in a single or multi-mesh LC networks called pulse-forming-network (PNF) [23]. In the single LC network, a single inductor and a single capacitor are used. The capacitance is chosen to supply the required energy stored at a convenient voltage, whereas the inductance is chosen to prevent explosion of the flashlamp. In other cases, the circuit contains two or more LC networks in series. This situation is called a multi-mesh LC. It is used for more strict control of the pulse duration and to deliver a constant power over a defined pulse interval.

The basic mechanism of the flashlamp is as follows. At low values of voltage applied to the gas in the flashlamp, there is no current flow. However, a small amount of ionization is always present [22]. As the voltage is increased, the current remains zero until sufficiently high voltage known as the breakdown voltage is reached. This is the value at which a large number of gas molecules become ionized. After the breakdown voltage is reached, the

conductivity of the gas increases and the electrons are accelerated to ionize more molecules through collisions [23]. Thus, as the current increases, the resistance of the gas decreases. Due to the increasing current, the voltage required to maintain the discharge decreases.

Initialization of electrical conduction is one of the main steps of the working mechanism of flashlamps. This is achieved by triggering the electrical discharge of the gas filling the flashtube. Triggering begins with a spark which occurs between the electrodes. Because the voltage drop across this spark is much less than the voltage supplied by the external circuit, current starts to flow through the lamp.

As flashlamps produce high-intensity pulses of light by operating electrical discharges, a high-voltage power supply is required [24]. Typical power supplies have basically two sections. The main section provides a dc source to charge the main discharge capacitors and place a potential across the flashlamp electrodes. Trigger section in the supply initiates an arc by applying a voltage of 5-40 kV across the flashlamp anode, cathode and trigger probe [24]. Power supplies can be controlled with computer as in our work. The basics scheme of the whole system is illustrated in the Figure 3.1.
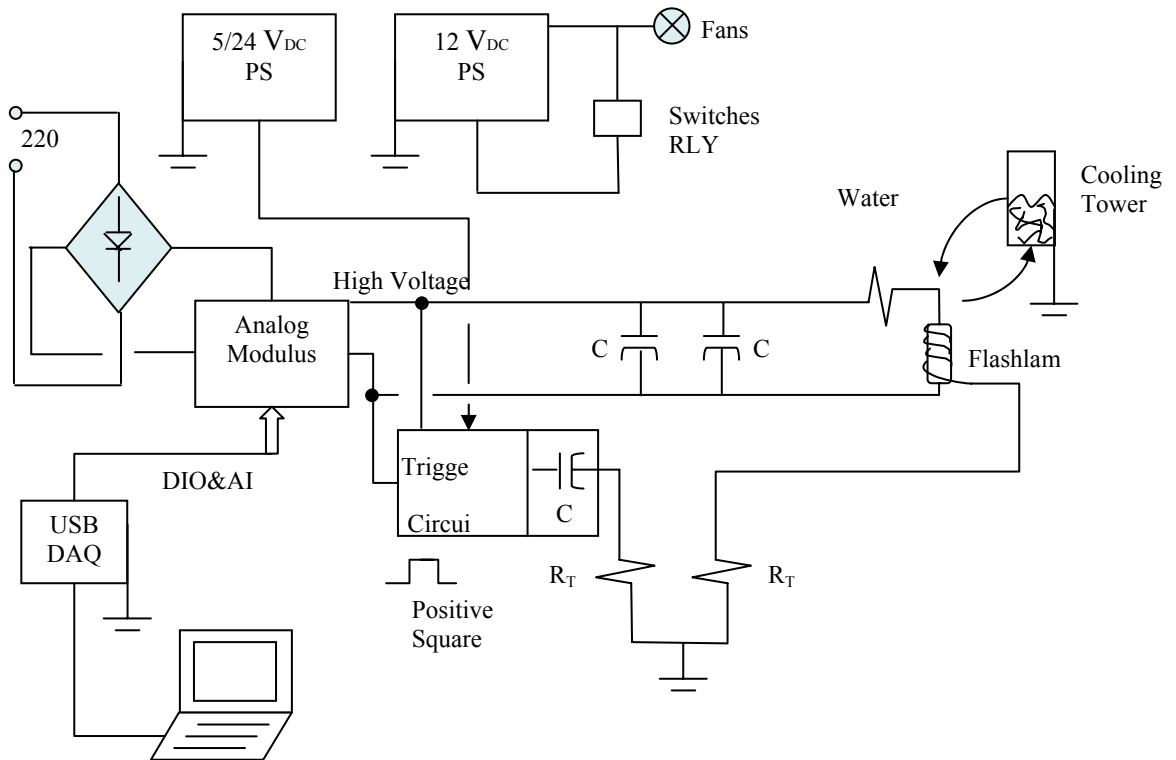
Figure 3.1: General schematic of our particular the flashlamp driver design.

12 V power supply was used for fans and 5/24 V power supply was used as a voltage source for the trigger circuit in the PFN. Capacitors, storing energy for transferring to the flashlamp, were supplied by 220 V AC. Computer was used as a controlling mechanism of the whole system. It was checking all components of the system that they were ready or not for operating. In addition, frequency of the square pulse which was directly related to the repetition rate of the flashlamp, voltage setting of the capacitors and working time of the system were specified with computer. A computer program was written in the Labview. Connection between software and hardware was achieved by USB DAQ which is an analog to digital and digital to analog converter.

On the other hand, in view of the features of the flashlamps, in order to use them as a pump source; pulse-forming-network (PFN) circuit has to be designed. Its basic structure can be seen in Figure 3.2.
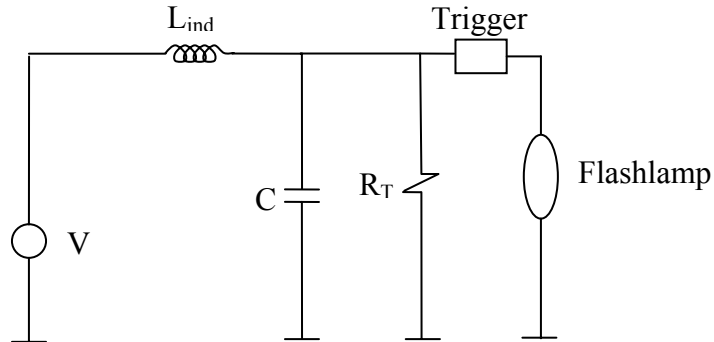
Figure 3.2: The basic Pulse-Forming-Network circuit.

This circuit performs a number of functions such as charging a capacitor that stores electrical charge until the flashlamp is ready to fire, controlling the flow of current, pulse shaping. The trigger initiates the electrical discharge in the flashlamp and enables the transfer of the energy stored in the capacitors. The basic schematic of the trigger circuit can be seen in Figure 3.3.
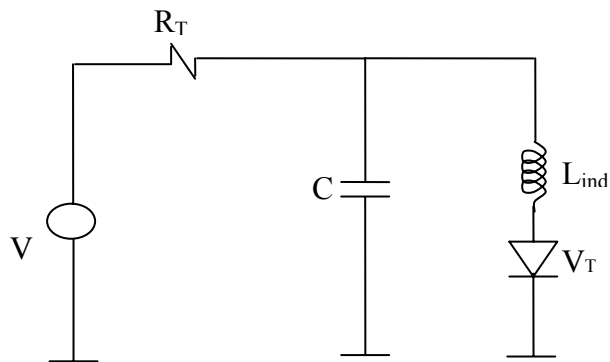
Figure 3.3: The basic schematic of the trigger circuit.

The fundamental mechanism of the pulse-forming-network can be summarized as follows: Capacitors are charged by a power supply at V_S. Pulse capacitor holds the charge until the pulse is created. Then, the trigger circuit delivers a high-voltage pulse that breaks down the flashlamp and starts the current flow. Following the discharge, energy storing capacitors discharge through the flashlamp.

The pulse shape and output energy of the flashlamp are controlled by the capacitance and inductance of the PFN as well as the lamp impedance. Hence the design involves two steps. In the first step the target pulse energy and pulsewidth are decided. In the second step, for given lamp impedance the capacitance and inductance values which gave the desired pulse energy and pulsewidth are calculated. The details of the calculation procedure are described in the next section.

3.2   Pulse Forming Network Calculations

In the analysis of the PFN, since the variations in the desired output energy and pulsewidth are not very strict, a single-mesh LC discharge circuit is considered for simplicity. The flashlamp is a non-linear circuit component whose resistance varies considerably during the charging process. Thus, impedance parameter (K_0), which depends on the type of the gas inside the tube, gas filling pressure, arc-length and the diameter of the tube, becomes important. These parameters can be obtained from the producer of the xenon flashlamp or can be calculated with empirically tabulated data or measurements [13]. The capacitance of the capacitor, impedance of the lamp, desired output energy, and pulse duration can be found for our specific design in table 3.1.

Output Energies (E_0) (for the first part)	8 J and 10 J
Pulse Duration (t_p) (for the second part)	200 μs
Single Capacitor	31.5 μF
Capacitors in Series($C_{ST} = C/2$)	15.7 μF
Capacitors in Parallel ($C_{PT} = 2C$)	63 μF
Lamp-impedance parameter (K_0)	17.6 Ω(Amp)$^{1/2}$

Table 3.1: Parameter values of the PFN.

Looking at table 3.1, it is not yet determined which voltage and inductance values will be used. In addition, the specific capacitor combination is also unknown. In order to determine these, the calculation procedure is divided into two steps which are described below. In both of them, calculations were repeated for all the capacitor values given in table 3.1.

In the first part of the calculations, the target output energy is fixed. The required voltage value was calculated for each capacitor combination by using the equation

$$V = \left(\frac{2E_0}{C} \right)^{1/2} ,$$
(3.1)

where E_0 is the output energy delivered to the flashlamp and C is the capacitance of the capacitor in the PFN circuit.

The fixed energy and capacitor values were later used to determine the pulsewidth of the light coming from the flashlamp from

$$t_p = \left(\frac{C^3 \times K_0^4}{0.09 \times E_0} \right)^{\frac{1}{2}} .$$
(3.2)

In the above equation, K_0 is the impedance parameter of the flashlamp filled with xenon gas. Indeed, as was shown in the original reference, t_p is also the pulsewidth of the current pulse through the flashlamp [13].

Finally, the inductance of the circuit could be obtained by the following expression [13]:

$$L_{ind} = \frac{t_p^2}{9 \times C},$$ (3.3)

where t_p is the pulsewidth of the output pulse and C is the capacitance of the circuit. Inductance calculations were done for each capacitance value given in table 3.1.

Different from the first part, the pulse duration is fixed in the second part of the analysis. Procedure is nearly same. Firstly, output energy was calculated again for each one of the capacitor combinations by using equation 3.2. Then, three voltage values were estimated for three different capacitor values by using calculated output energy in the equation 3.1. Finally, necessary inductor value was calculated with equation 3.3 for each capacitor values and fixed pulse duration.

By using the three simple design equations listed above, the specific capacitor combination which provides the desired operating parameters can be determined. Summaries of the PFN analysis can be found in tables 3.2, 3.3 and 3.4. Initial values are in the first line and results are in the second line for both parts of the calculations in tables.

Initial Parameters:				Results	
E_0 (J)	C_T (μ F)	K_0 (Ω(Amp)$^{1/2}$)	V (volt)	tp (μ s)	L_{ind} (μ F)
8	63	17.6	504	183	59
8	31.5	17.6	713	65	15
8	15.7	17.6	1010	23	4

Table 3.2: Summary of the part1 of the analysis for the output energy fixed at 8 J.

Initial Parameters:				Results	
E_0 (J)	C_T (μ F)	K_0 (Ω(Amp)$^{1/2}$)	V (volt)	tp (μ s)	L_{ind} (μ F)
10	63	17.6	563	163	47
10	31.5	17.6	797	58	12
10	15.7	17.6	1129	20	3

Table 3.3: Summary of the part1 of the analysis for the output energy fixed at 10 J.

Initial Parameters:				Results	
tp (μ s)	C_T (μ F)	K_0 (Ω(Amp)$^{1/2}$)	V (volt)	E_0 (J)	L_{ind} (μ F)
200	63	17.6	463	6.7	71
200	31.5	17.6	230	0.83	141
200	15.7	17.6	115	0.103	283

Table 3.4: Summary of the part 2 of analysis for the pulsewidth fixed at 200 μs.

For the first part of the analysis, calculations as described above were done for two fixed output energies which are 8 J and 10 J. For 8 J output energy, it was found that the parallel combination of capacitors ($C = 31.5$ μF for each capacitor) was the suitable choice. This is because the calculated pulsewidth of 183 μs comes very close to the desired value of 200 μs (see table 3.2). In addition, the required voltage was calculated to be around 504 V which is reasonable for our design. For 10 J output energy, the calculated pulsewidth and voltage came to 163 μs and 563 V, respectively. As it can be seen, parallel combination of capacitor was the suitable choice in our particular design.

In the second part of the calculations, pulsewidth as in the previous part and impedance of the flashlamp are fixed. If the results are considered, it can be seen that parallel case for capacitors are suitable combination for desired PNF circuit. The voltage is 463 V which is convenient for our design and the energy coming out from flashlamp is calculated as 6.7 J. This is close to the desired output energy of 8 J.

During flashlamp operation by using the designed driver at a pulse repetition rate of 1 Hz, the pulse profile of the output pulses from the flashlamp was recorded with a high-speed silicon detector (DET200) and a fast oscilloscope (EZ Digital Oscilloscope DS-1250 250 MHz) with 50 Ω terminations. The applied voltage was 563 V. The pulsewidth was measured to be 150 μs. The temporal profile of the pump pulse is shown in Figure 3.4. The horizontal axis has a calibration of 0.1 ms per division. As it can be seen in Table 3.3, the calculated pulsewidth is 163 μs. The percentage error was 8.6 %, indicating that calculations were in good agreement with the measurements.
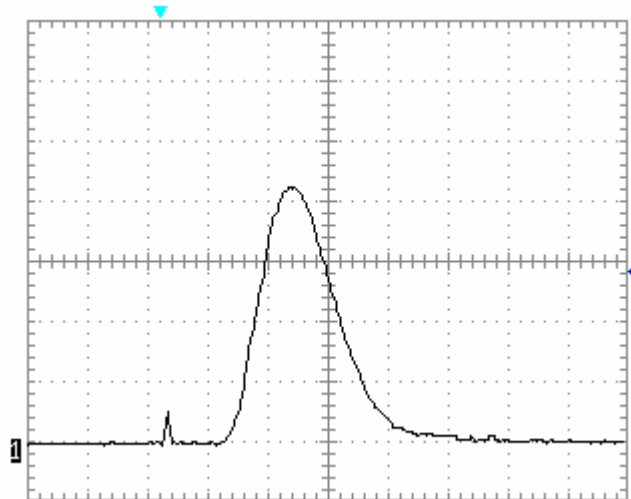
Figure 3.4: Measured temporal profile of the output pulses from the flashlamp. The pulsewidth was obtained to be 150 μs where the horizontal axis has a calibration of 0.1 ms per division.

3.3   The Air Cored Coil

An inductor, which does not depend on a ferromagnetic material to achieve its specific inductance, is called air core coil. There is just air inside instead of different insulators such as; bakelite or glass. Thus, the energy loss is much lower than the other inductors wound around an insulator. Air cored coil can be designed to perform at high frequencies such as 1 GHz. Moreover, its inductance is not affected by the current passing from the wires and it is free from the non-linearity. Mainly, single layer and multi layer air cored coil are the two types of it. In the PNF circuit, there is an inductor whose inductance is determined for required output energies and capacitor values.

The quality (Q) factor of a coil is important parameter due to effect the sharpness of the response curve. The Q-factor of a resonant circuit is the ratio of the energy stored in it to the energy lost during one cycle of operation. For air cored coil energy loss is not high as much as other inductors. Thus, a better Q-factor could be obtained.

3.3.1   Single Air Coil

As can be seen from its name, a single layer air cored coil has only one winding. This type of air cored coil has the added advantage of low self capacitance. In the simple case of a single layer solenoid coil, the inductance can be estimated as follows [24, 25]:

$$L_{ind} = \frac{0.001 \times N^2 \times r^2}{(228r + 254l)} .$$
(3.4)

Here, L_{ind} is the inductance in henrys, r is the coil radius in meters, l is the coil length in meters and N is the number of turns. As it can be seen from the equation, inductance is related to the square of the number of turns. After fixing the radius of the coil, the inductance is adjusted by increasing and decreasing the number of turns.

3.3.2 Calculations

In PFN calculations, in section 3.2, it was estimated that parallel combination was the suitable case for the desired values. The calculated inductances are 59 μH and 47 μH for 8 J and 10 J output energies, respectively. For the second part of the calculations, L_{ind} was determined as 71 μH. The number of turns needed to achieve this inductance was estimated by using equation 3.4. In the inductance calculation the radius was kept fixed at 2.85 cm. Three particular coil lengths of 2×10^{-2} m, 3×10^{-2} m and 4×10^{-2} m were tried. The resultant number of turns for these three inductances can be seen in the table 3.5.

	Initial Values		Resultant Number of Turns
r (coil radius)	l (coil length)	L_{ind} (Inductance)	
2.85×10^{-2} m	2×10^{-2} m	47×10^{-6} H	26 turns
2.85×10^{-2} m	3×10^{-2} m	47×10^{-6} H	29 turns
2.85×10^{-2} m	4×10^{-2} m	47×10^{-6} H	31 turns
2.85×10^{-2} m	2×10^{-2} m	59×10^{-6} H	29 turns
2.85×10^{-2} m	3×10^{-2} m	59×10^{-6} H	32 turns
2.85×10^{-2} m	4×10^{-2} m	59×10^{-6} H	35 turns
2.85×10^{-2} m	2×10^{-2} m	71×10^{-6} H	32 turns
2.85×10^{-2} m	3×10^{-2} m	71×10^{-6} H	35 turns
2.85×10^{-2} m	4×10^{-2} m	71×10^{-6} H	38 turns

Table 3.5: Summary of calculated values of number of turns for the desired inductance values of 47, 59, 71 μH.

From results of air cored coil calculations, it can be seen that when an inductor is being wound, the number of turns should be about 30. In addition, as the energy can be changed by voltage, it was decided that the results for 10 J output energies could be used for the construction of the inductor. Reviewing the results and initial parameters, an inductor with

a length of 4.3×10^{-2} m and a radius of 2.85×10^{-2} m was built. After winding the inductor, the inductance value and Q-factor were checked by digital LRC meter (model: MIT 9216A). The measured inductance value came to 63×10^{-6} H. The percentage error was 34%.

3.4   Simulations

In order to test the performance of the PFN, the parameters were used in the Spice circuit simulation program. In the test, voltage was changed from 400 to 700 V in 10 V steps. The program was run for two inductance values of 59 and 47 μH. In graphs, the energy, power and resistance were calculated for each voltage. The results can be found in Figure 3.5 for 59 μH and in Figure 3.6 for 47 μH.
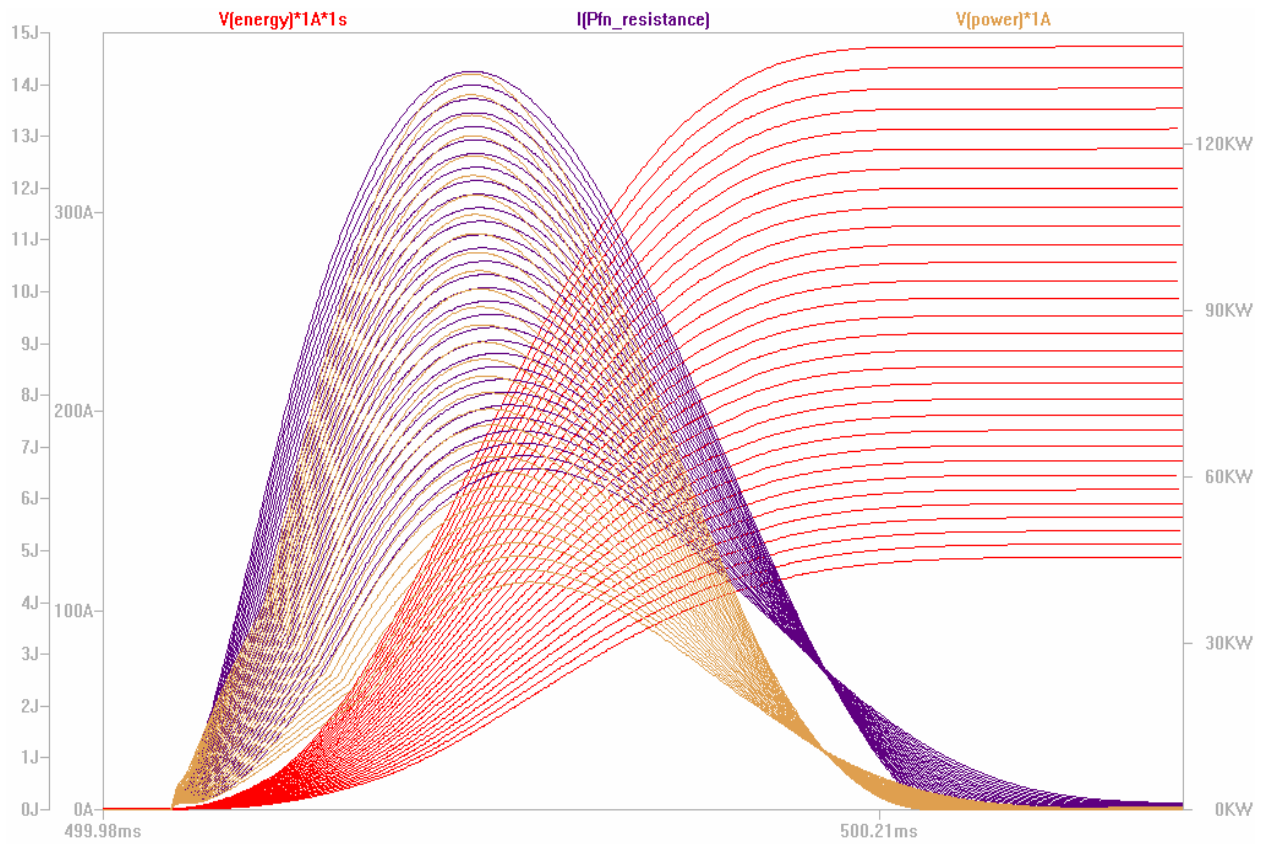
Figure 3.5: Graph of energy, current and power versus time for inductance value of 59 μH.
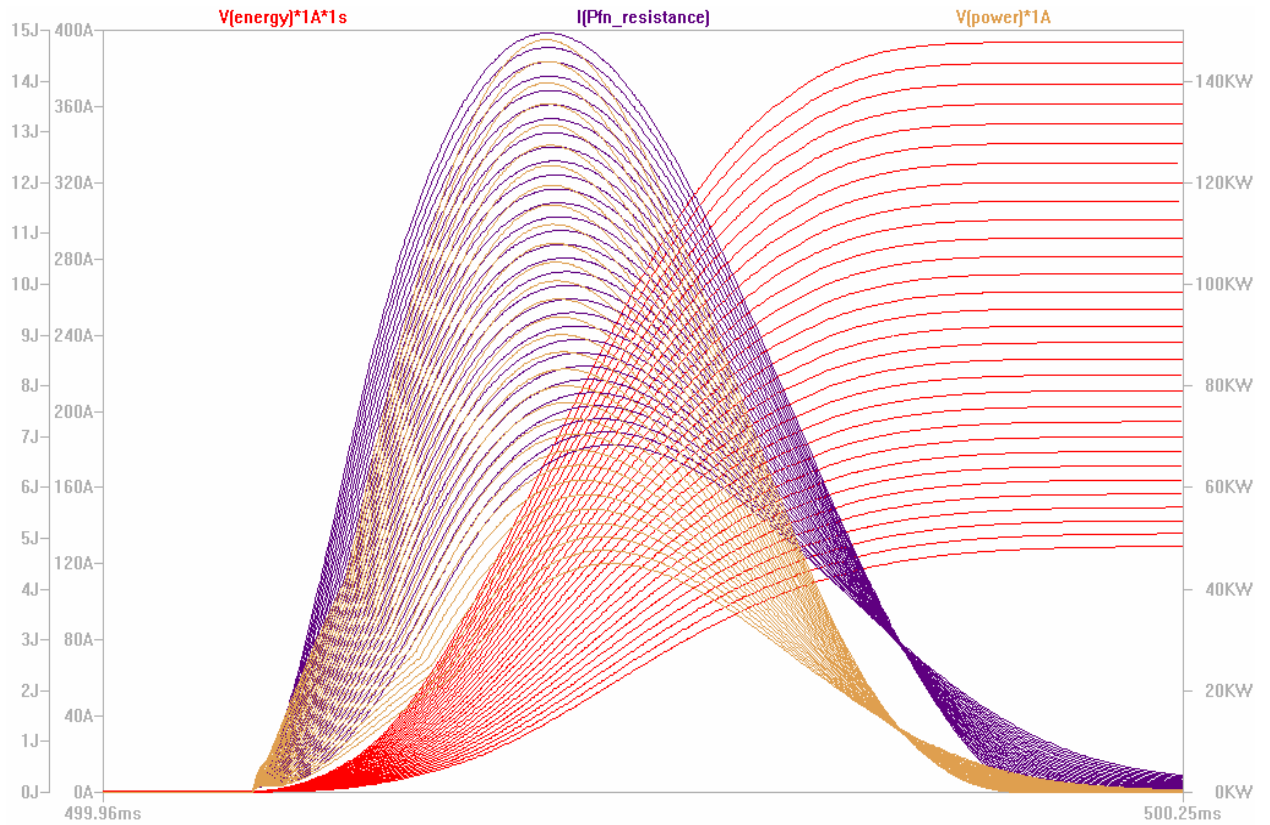
Figure 3.6: Graph of energy, current and power versus time for inductance value of 47 μH.

As it can be seen from the figures, the results from simulations and from calculations are in very good agreement. For instance, according to equations 3.1-3.3, the desired output energy should be 8 J for 59 μH inductor at 504 V. From Figure 3.5, it can be seen that at the energy of 8 J, the voltage is nearly 540 V. Similarly, for the other desired output energy of 10 J for 47 μH inductor, the design equation gave a voltage of 563 V. If it is checked from Figure 3.6, it is seen that the voltage is nearly 590 V for 10 J and 47 μH case, again in good agreement.

Chapter 4

1572-nm KTP OPTICAL PARAMENTRIC OSCILLATOR (OPO) EXCITED BY A FLASHLAMP PUMPED Nd:YAG LASER AT 1064 nm

4.1   Flashlamp Pumped Nd:YAG Laser

Nd:YAG is a four-level optical gain medium. The upper energy levels are populated by pumping the Nd^{3+} ions with light near 720 nm and 830 nm. In order to pump ions from ground-state flashlamps or GaAlAs diode lasers can be used. The pumping creates a population inversion in the upper energy level. The Nd^{3+} ions fall down very fast from the upper energy levels to the upper laser level. Then, from this upper laser level lasing occurs by the transition from $^4F_{3/2}$ to $^4I_{11/2}$ and radiated light is at 1.064 μm [26]. After all, the ions fall back very fast to the ground state from the lower laser level. Nd:YAG lasers can be operated either in pulsed or continuous wave (CW) modes.

In our system, Nd:YAG laser was operated in the pulsed mode. As a pumping source flashlamp was used and in order to run it a driver, described in the first part, was constructed and characterized. The cavity of Nd:YAG laser consisted of two end mirrors. Mirror M1 (HR 99.8% at 1.064 μm, r_c = 100 cm) was used as a first mirror and mirror M2 (PR 50% at 1.064 μm, flat) was used as an output coupler for laser resonator. In addition, Nd:YAG rod was kept at room temperature by using water cooling. The configuration and details of the 1.064-μm Nd:YAG laser can be found in Figure 4.1 below.

M1: Plano/curve, radius = 100 cm, HR at 1064-nm.
M2: Plano/plano, PR 50% at 1064-nm.
C1: Nd:YAG (6x76 mm, 0.9% Nd and AR@1064-nm).
Cham: Flashlamp chamber.
L: 32.5 cm, L1: 7.5 cm, L2: 17.4 cm.
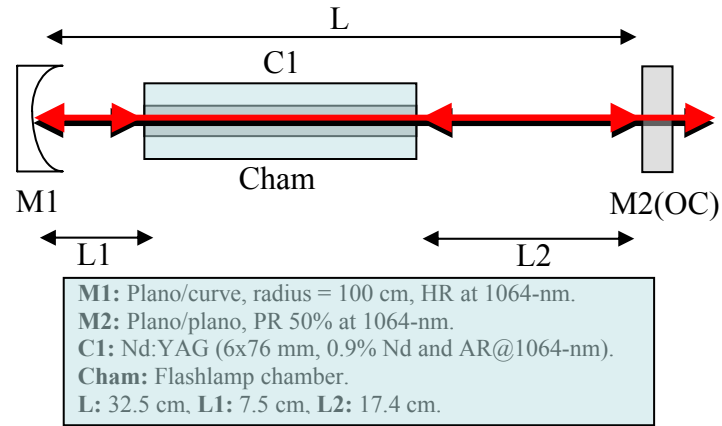
Figure 4.1: The schema of the flashlamp pumped Nd:YAG laser operating in the long pulse mode.

The efficiency graphs of the Nd:YAG laser operating in the long-pulse mode (output energy as a function of input energy and output energy as a function of voltage) are shown in Figures 4.2 and 4.3, respectively. In the first graph, input energies coming from flashlamp were estimated for every voltage value, applied to the flashlamp, by using basic equation 3.1, described in the third chapter.
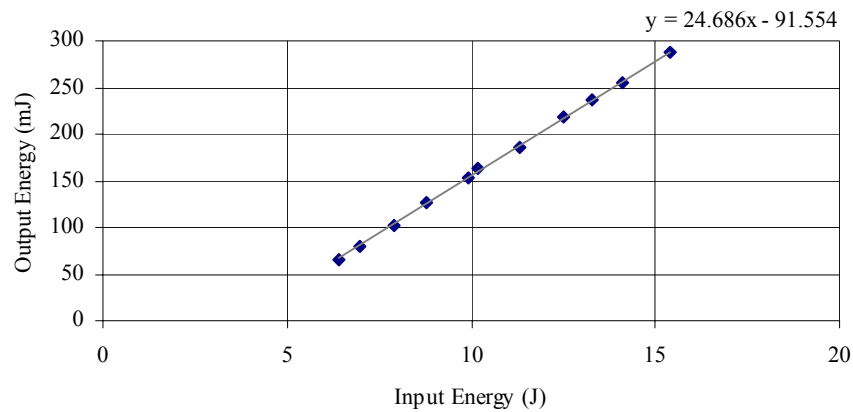
Figure 4.2: Efficiency graph of the Nd:YAG laser showing the output energy as a function the input energy.
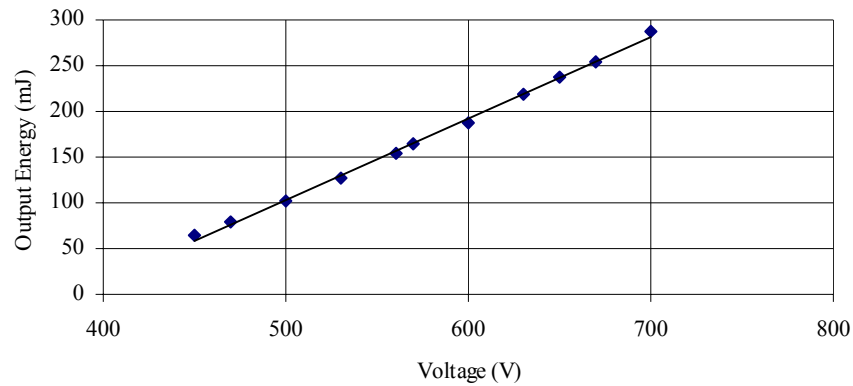
Figure 4.3: Efficiency graph of the Nd:YAG laser showing output energy as a function of the voltage.

By using the 50% output coupler and with about 15.4 J of input electrical energy (applied voltage = 700 V), about 290 mJ of output energy was obtained at 1.064 μm in the long-pulse mode. The slope efficiency of the laser was estimated to be 2.47%. The pulsewidth of the 1.064 µm Nd:YAG laser operating in the long-pulse mode was measured to be 220 μs. The pulse profile was recorded with a high-speed silicon detector (DET200) and a fast oscilloscope (EZ Digital Oscilloscope DS-1250 250 MHz) with 10 kΩ terminations. Figure 3.4 shows the temporal pulse profile of the laser system. The horizontal axis has a calibration of 0.1 ms per division.

For passive Q-switching, a Cr^{4+}:YAG crystal was used as a saturable absorber. One of the reasons of using this crystal for passive Q-switching in the Nd:YAG laser is that the emission band of the Nd:YAG laser at 1.064 μm overlaps with the absorption band of Cr^{4+}:YAG crystal ($^3A_2 \rightarrow {}^3T_2$) [19]. The other reason is that Cr^{4+}:YAG crystal has low excited state absorption value. Thus, this reduces the loss in the laser cavity. It has a small signal transmission of 50% and is antireflection coated at 1.064 μm. Thus, it was positioned at normal incidence inside the laser cavity. The configuration and details of the system are illustrated in Figure 4.5.
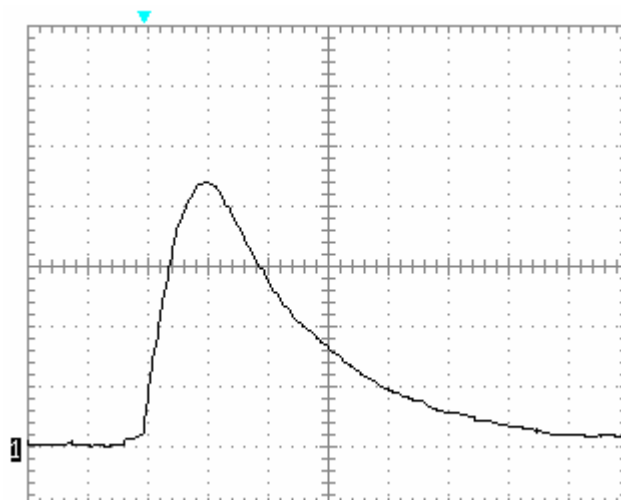
Figure 4.4: The temporal profile of the output pulses from the Nd:YAG laser at 1.064 μm operating in the long-pulse mode. The pulsewidth was determined to be 220 μs where the horizontal axis has a calibration of 0.1 ms per division.

M1: Plano/curve, radius = 100 cm, HR at 1064-nm.
M2: Plano/plano, PR 50% at 1064-nm.
C1: Nd:YAG (6x76 mm, 0.9% Nd and AR@1064-nm).
C2: Cr:YAG, dia = 10 cm, T = 50% at 1064-nm.
S7: Plane parallel window at Brewster angle.
Cham: Flashlamp chamber.
L_T: 32.5 cm, **L1:** 7.5 cm, **L2:** 17.4 cm, **L3:** 7.5 cm, **L4:** 5.5 cm.
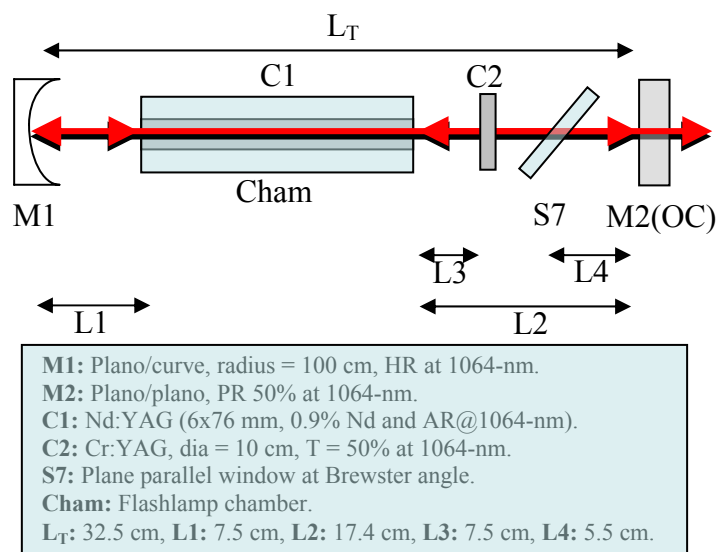
Figure 4.5: The schema of the flashlamp pumped Nd:YAG laser with Cr^{4+}:YAG as a saturable absorber.

As seen in Figure 4.5, an uncoated, polished glass window was placed inside the resonator at Brewster incidence. This introduces more loss for the field component perpendicular to the plane of Figure 4.5 and makes the output of the laser linearly polarized. Since the efficiency of the parametric signal generation is polarization dependent, the linearly polarized output of the laser can be adjusted to maximize the OPO output. Without the Brewster plate, the output of the laser would be un-polarized and OPO efficiency would be significantly reduced.

During passively Q-switched operation, single output pulse energies of 67 mJ were obtained on average at a pulse repetition rate of 1 Hz, when a voltage of 570 V was applied to the flashlamp. The pumping energy was estimated to be 10 J by assuming a capacitance value of 63 μF and by using equation 3.1. A single Q-switched pulse is shown in Figure 4.6. A high-speed InGaAs photodiode and Tektronix Oscilloscope (TDS-350 200 MHz) with 10 kΩ termination were used in the recording of the temporal profile of the single Q-switched pulse. Figure 4.7 shows the temporal profile of the output pulses from the Nd:YAG laser. The pulsewidth was measured to be 117 ns. The pulse profile was recorded with a high-speed silicon detector (DET200) and a fast oscilloscope (EZ Digital Oscilloscope DS-1250 250 MHz) with 50 Ω terminations.

The peak power of the laser can be determine by using the equation

$$P_{peak} = \frac{E}{\tau_p},$$
(4.1)

where E is the output energy and τ_p is the pulsewidth of the single output pulse. In this particular case the peak output power was determined to be 573 kW.
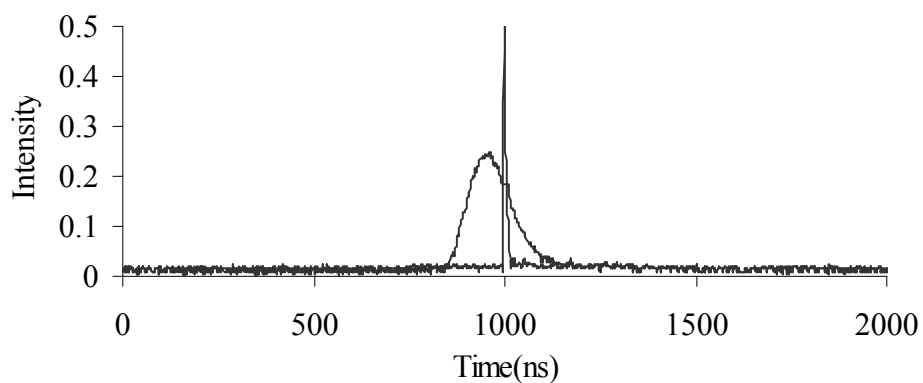
Figure 4.6: Single pulse from 1064-nm Nd:YAG laser operating in the Q-switching mode when the input pump energy was 10 J. The broad pulse preceding the single pulse shows the temporal trace of the flashlamp pulse.
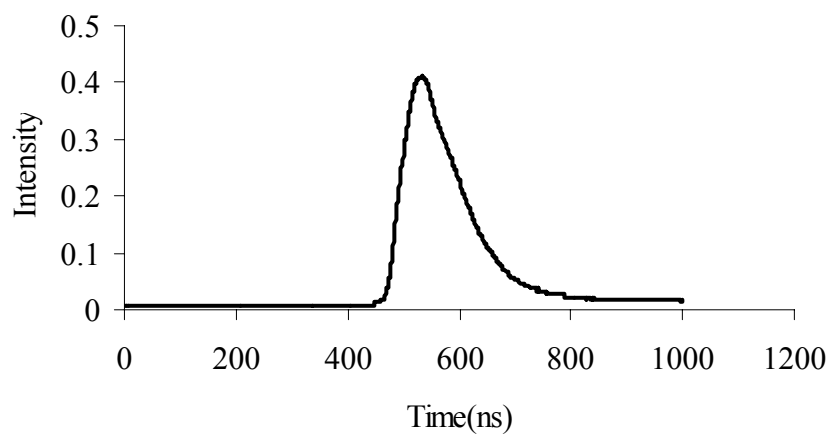
Figure 4.7: The temporal profile of the output pulses from the passively Q-switched Nd:YAG laser at 1.064 μm. The pulsewidth was determined to be 117 ns.

4.1.1   Comparison of Experimental Results with Theoretical Predictions of 1064-nm Nd:YAG Laser Operating in Q-switching Mode

In the chapter 2, rate equations were derived by two methodologies described in references [10] and [11]. In both of methods, plane-wave approximation was used. Due to the transcendental nature of the rate equations, they solved numerically. The Q-switched performance of 1064-nm Nd:YAG laser was optimized in terms of output energy and pulsewidth. In this section, numerical predictions have been discussed and compared with experimental results.

In table 4.1 [13, 15-19, 21] below, cavity parameters, gain medium parameters and saturable absorber parameters (Cr:YAG) used in numerical calculations of the rate equations for both methods are listed, respectively.

Cavity Parameters	Symbol	Units	Value
length of the cavity	l_c	cm	32.2
reflectivity of the OC	R		0.54
one way transmission	T_{ow}		0.99
loss	L		0.03

(a)

Nd:YAG Parameters	Symbol	Units	Value
emission cross-section	σ_e	cm^2	6.5×10^{-19}
lentgh of the gain medium	l_g	cm	7.6
laser wavelength	λ	nm	1064
effective area	A	cm^2	0.312
refractive index	n_g		1.82
inversion reduction factor	γ		0.7

(b)

Cr^{4+}:YAG Parameters	Symbol	Units	Value
GSA	σ_{gsa}	cm^2	$10\text{-}50 \times 10^{-19}$
ESA	σ_{esa}	cm^2	$2 \pm 0.2 \times 10^{-19}$
length of the SA	l_{sa}	cm	0.3
refractive index	n_{sa}		1.81
initial transmission	T_0		0.5
inversion reduction factor	γ_{SA}		0.9

(c)

Table 4.1: Cavity (a), gain medium (b), and saturable absorber (c) parameters used in the numerical calculations of passively Q-switched 1064-nm Nd:YAG laser with Cr:YAG as a saturable absorber.

Numerical calculations demonstrated that the best agreement with experimental results from $L = 3\%$. The experimental results obtained from the passively Q-switched 1064-nm Nd:YAG laser (see: Figure 4.5) described in the previous section were compared with the theoretical predictions in Table 4.2 below.

Experiment		Theory			
		Degnan		Zhang	
E_o (mJ)	t_p (ns)	E_o (mJ)	t_p (ns)	E_o (mJ)	t_p (ns)
65-75	117ns	68.5	99.2	68.7	106.9

Table 4.2: Comparison of experimental and theoretical output energy and pulsewidth of single pulses from 1064-nm Nd:YAG laser operating in the Q-switching mode.

As seen in Table 4.2, the energy and pulsewidth values predicted by the theory are in good agreement with experimentally observed results for the 1314-nm Nd:YAG laser passively Q-switched by the Co:MALO crystal (with in the experimental error limits).

4.1.2   The Telescope for the KTP OPO Set-up

In order to use passively q-switched Nd:YAG laser as a pump source for extra-cavity KTP OPO, we needed to reduce the spot size of the pump light. This is because, the spot radius of the light coming from Nd:YAG was nearly 3 mm. Thus, in front of the Nd:YAG laser a telescope was set-up. The configuration of the telescope is shown in Figure 4.8.

Looking at Figure 4.7, the first lens is a converging lens with 20 cm focal length and the second one is a diverging lens with -5 cm focal length. Both of them are antireflection coated at 1.064 μm. Ideally the distance between these lenses should be 15 cm so that the spot size of the beam can be reduced by the ratio of the focal lengths which is ¼ in our case. However, because the light coming out from the Nd:YAG laser was transverse multi-mode, the optimum telescope separation was determined by minimizing the beam radius after telescope. As can be seen in the Figure 4.8, the distance L between the lenses was approximately 20.8 cm.

f = 20 cm   f = - 5 cm

L = 20.8 cm
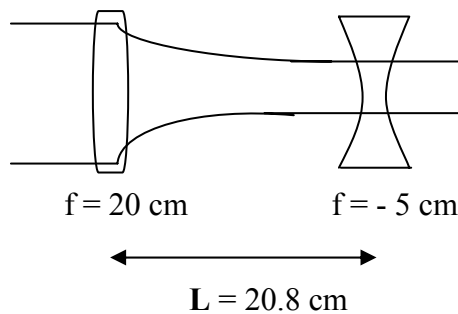
Figure 4.8: The schematic of the telescope used in the extra-cavity KTP OPO setup.

In order to figure out the spotsize profile of the passively q-switched Nd:YAG laser and telescope system as a function of position, spot size of the beam was recorded at 12 different positions. In the measurement of the spot sizes, Polaroid films were used. From the marks on the films, it was observed that laser beam was elliptic. The radii of the semi minor and semi major axis of the ellipses are shown in Figure 4.9. The variation of the beam area as a function of position was determined by using the well know formula

$$Area = \pi \times r_{small} \times r_{big} \text{ ,} \qquad\qquad (4.2)$$

for the ellipse.
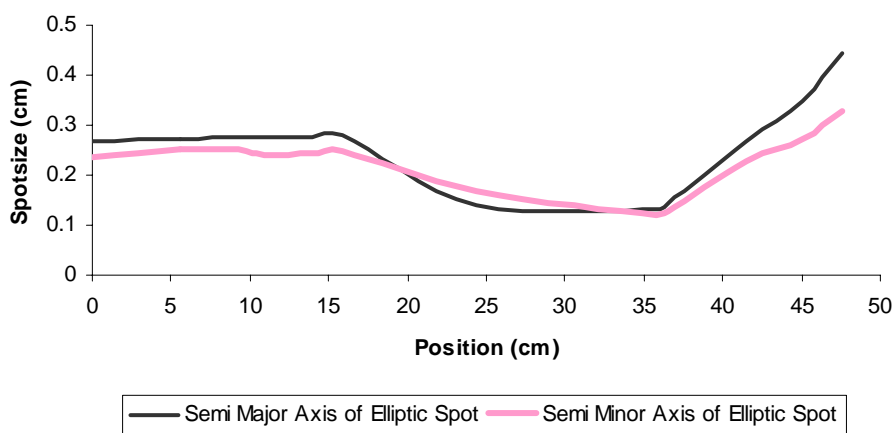
Figure 4.9: Measured variation of the elliptic radii as a function of position. The origin corresponds to the location of the output coupler.
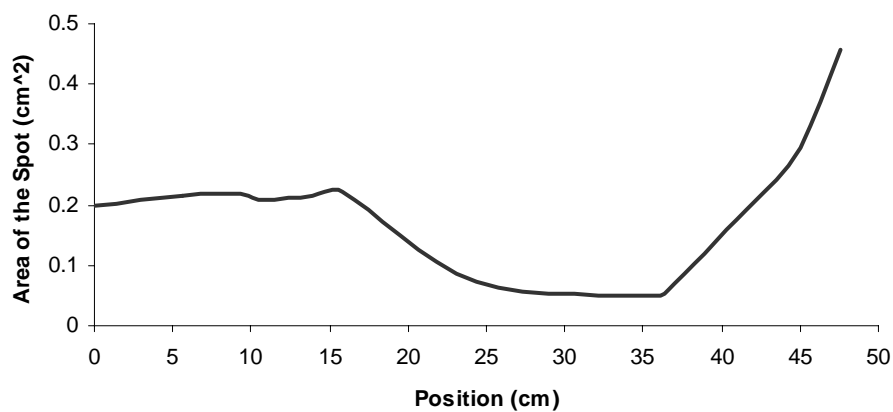
Figure 4.10: Measured variation of the beam area as a function of position. The origin corresponds to the location of the output coupler.

4.2   KTP Optical Parametric Oscillator (OPO)

Optical parametric generation depends on the second-order non-linear response of a medium. During this process, the medium (usually a crystal) converts the high energy photon into two lower energy photons.

Due to the conversion of energy, the three photon wavelengths are related as follows

$$\frac{1}{pumpwavelength} = \frac{1}{signalwavelength} + \frac{1}{idlerwavelength}. \tag{4.3}$$

The actual wavelengths of the signal and idler beams depend on the phase matching conditions. Energy can be transferred efficiently to the parametric waves if all three waves are traveling at the same velocity [26]. When the crystal is placed in a resonator, feedback causes gain in the parametric waves. Thus, the signal and/or the idler can be made to resonate. One of the configurations for KTP optical parametric devices is the singly resonant OPO, where only the signal oscillates. Figure 4.11 illustrates this configuration.
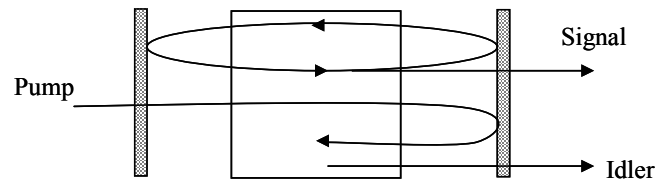
Figure 4.11: The schematic of the singly resonant OPO.

The singly resonant OPO is one of the most common configurations due to the several advantages such as: ease of resonator design, good conversion efficiency and frequency stability [13]. Moreover, the threshold can be reduced easily by double passing the pump beam through the non-linear crystal. For this type of configuration, on the other hand, damaging the crystal may become one of the problems due to the high power density [13].

The input mirror was highly reflective (R = 99.8%) at 1.570 μm and highly transmitting at 1.064 μm. The output coupler was highly reflective (R = 99.8%) at 1.064 μm and partially reflective (R = 90%) at 1.570 μm. The radius of the output coupler was 10 cm. The length of the OPO resonator was 2.25 cm. The KTP crystal was positioned as close to the second lens of the telescope as was allowed by the mirror holders. The half wave plate at 1.064 μm (HWP) was used to rotate the pump polarization and optimize the parametric generation efficiency. Rotating the pump polarization was more practical in our case in comparison with rotating KTP crystal itself. Filter (F) only lets the signal through and blokes the pump as well as the idler beams. The whole system, the details of the components and the positions are shown in Figure 4.12. The photograph of the whole system can be seen in Figure 4.13.

FLPNdYAG*: Flashlamp pumped NdYAG, see figure 4.5.
M1: Plano/Plano, HR at 1570 nm.
M2: Plano/Concave, radius = 0.1m, PR=90% at 1570 nm.
C1: KTP crystal (7x7x20mm; $\Phi = 0^0$, AR at 1064 4 1570 nm).
L1: 9.8 cm, L2: 5.8 cm, L3: 20.8 cm, L4: 3cm, L5: 0.1 cm, L6: 0.15 cm, L7: 2.25 cm, L8: 11 cm.
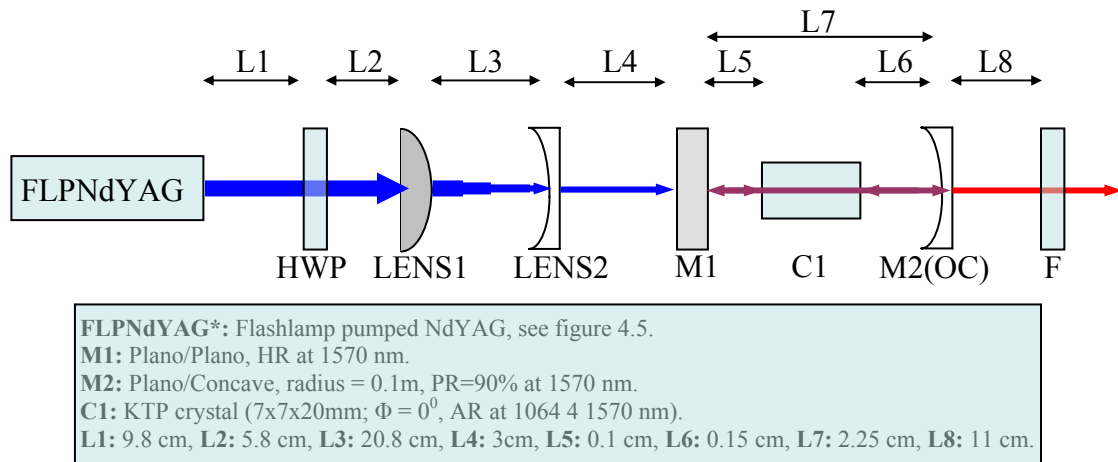
Figure 4.12: The schematic of the Nd:YAG pumped eye-safe KTP OPO setup.
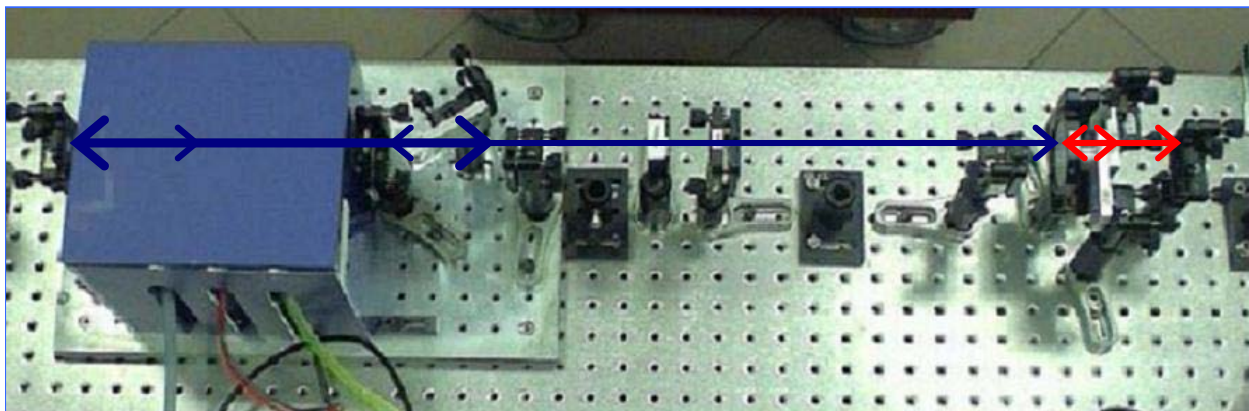
Figure 4.13: The photograph of the Nd:YAG pumped eye-safe KTP OPO setup.

In this configuration, output energies of approximately 8.2 mJ were obtained at 1.572 μm when a voltage of 560 V was applied to the flashlamp. The output wavelength of the KTP OPO was measured with ¼ meter monochromator. By using the high-speed InGaAs photodiode, the output pulsewidth was measured to be 79 ns. The temporal profile of the eye-safe pulse is shown in Figure 4.14.
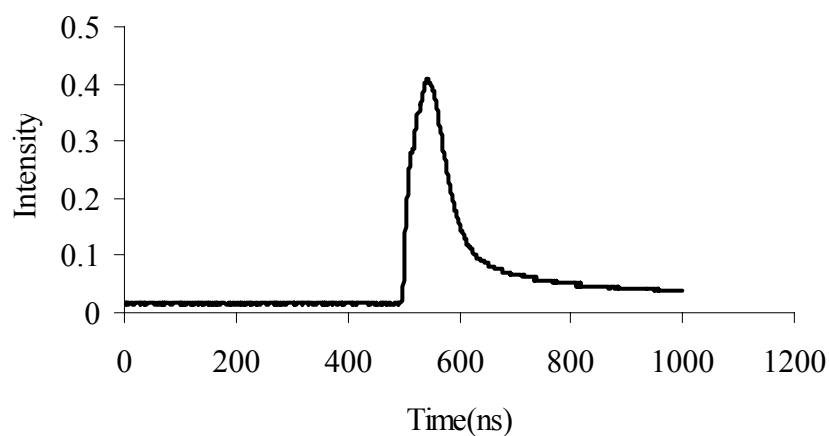
Figure 4.14: Measured temporal profile of the KTP OPO output pulses at 1.572 μm.

4.3   Intensity Calculations

In order to avoid the damage of optical components, it is important to calculate the beam intensities and make sure that they remain below the damage thresholds. For instance, in OPO configuration (see: Figure 4.11), non-linear KTP crystal was damaged when it was put 0.7 cm away from diverging lens. However, after the distance between diverging lens and crystal was increased to 3 cm, OPO generation could be obtained safely.

In order to estimate intensities for specific positions, the area of the spot versus position graph of the Nd:YAG laser and the telescope system (see: Figure 4.10) could be used. In order to find out the intensity of the coming laser beam at the location where the non-linear KTP crystal was damaged, equation 4.1 was used to calculate the peak power. Then, calculated peak power was divided by the area of the beam to determine the by using

$$I = \frac{P_{peak}}{AreaOfBeam} .$$

(4.4)

Measured variation of the beam area as a function of position is shown in Figure 4.10. Damage to the KTP crystal occurred at 37.1 cm away from the output coupler of the Nd:YAG laser, where the area of the laser beam was 0.08 cm^2. KTP OPO worked properly and safely when the crystal was positioned approximately 39.5 cm away from the Nd:YAG output coupler. Here, the area of the pump light was 0.13 cm^2. The peak power of the Nd:YAG laser was calculated to be 5.73x10^5 W in the previous section. By using equation 4.4, the corresponding intensities at 37.1 cm and 39.5 cm were determined to be 7.16x10^6 W/cm^2 and 4.4x10^6 W/cm^2, respectively.

Damage threshold intensity of the KTP crystal at 1.064-μm is reported to be 500x10^6 W/cm^2 [27]. Thus, this suggests that, the cause of the damage is not the pump beam but the intra-cavity OPO beam. So the intra-cavity intensity of the OPO was further estimated.

L5: 0.1 cm, L6: 0.15 cm, L7: 2.25
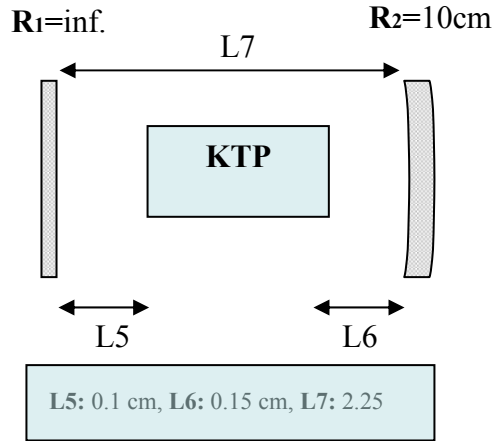
Figure 4.15: The schematic of the KTP OPO.

The schematic of the KTP OPO cavity is as shown in Figure 4.15. The procedure of the intensity calculation for the OPO is similar to what was described previously. The spot size at the first mirror can be estimated from the equation

$$w_1^2 = \frac{Leff \times \lambda}{\pi} \sqrt{\frac{g_2}{g_1(1-g_1g_2)}}, \tag{4.5}$$

where w_1 is the spot size of the beam and λ is the wavelength of the oscillating beam. The parameters g_1 and g_2 can be found from

$$g_1 = 1 - \frac{Leff}{R_1}, \tag{4.6}$$

$$g_2 = 1 - \frac{Leff}{R_2}, \tag{4.7}$$

where L_{eff} is the effective cavity length, R_1 and R_2 are the radii of the cavity mirrors. As the length of the crystal was 2 cm (see: Figure 4.15), effective length of the cavity should be determined as follows:

$$Leff = L5 + n_{KTP} \times L6 + L7 = 0.1 + 1.86 \times 2 + 0.15 = 3.97 cm, \tag{4.8}$$

where n_{KTP} is the index of reflection of KTP crystal [27]. With this value of L_{eff}, g_1 and g_2 were calculated to be 1 and 0.603, respectively. By using these calculated parameters the laser beam area at the first mirror was calculated to be 7.68×10^{-4} cm^2.

The actual energy coming out of the OPO was approximately 10 mJ. The output coupler had 10% transition. Thus, intra-cavity energy was 100 mJ. Peak power of the single pulse of the system was calculated to be 1.27×10^6 W by using equation 4.1. The corresponding intensity becomes 1.65 GW/cm^2. This result is in support of the fact that damage was caused mainly by the OPO beam rather than the Nd:YAG pump. Damage could also be due to the presence of hot spots in the beams.

Chapter 5

RAMAN AMPLIFICATION IN BARIUM NITRATE (Ba(NO$_3$)$_2$)

5.1   Theory of Raman Scattering

Mainly, three methods stand out for obtaining high-power laser radiation pulses in the 1.5-1.6 μm spectral region: direct lasing from solid-state laser media activated by erbium ions, nonlinear optical conversion of radiation, especially OPO in KTP crystal described in the previous report and stimulated Raman scattering (SRS) [13]. The basic Raman Effect is an inelastic light scattering process whereby light at one wavelength is converted to another wavelength [28]. In other words, the energy of an incident photon is modified by an inelastic interaction with the vibrating crystal ions.

The energy levels of Raman scattering are shown in Figure 5.1. u is the virtual upper state of the molecules, and i and f are the initial and final states or vibrational energy states. The frequency v_S is called Stokes frequency and the frequency v_{AS} is called anti-Stokes frequency. v_R and v_P are Raman shift and pump frequencies, respectively. The Raman Shift frequency is characteristic of the materials using in the Raman process [6]. For the spontaneous Raman Effect, the molecule will be excited from the initial state to a virtual energy state and relax into a vibrational excited state. Hence, Stokes Raman scattering is generated. Figure 5.1 (a) shows the process of Stokes Raman scattering. The difference between the pump frequency and Raman shift frequency gives Stokes frequency as follows

$$v_S = v_P - v_R.$$ (5.1)

As it can be seen from equation 5.1, Stokes frequency is smaller than the incident light frequency.

For a molecule already in an excited vibrational state (see: Figure 5.1 (b)), the reverse scattering process can take place. If the molecule is already in an elevated vibrational energy state, Raman scattering is then called anti-Stokes Raman scattering. This frequency is equal to

$$\nu_{AS} = \nu_P + \nu_R .$$ (5.2)

In that case, the scattering light has a higher frequency than the exciting light.
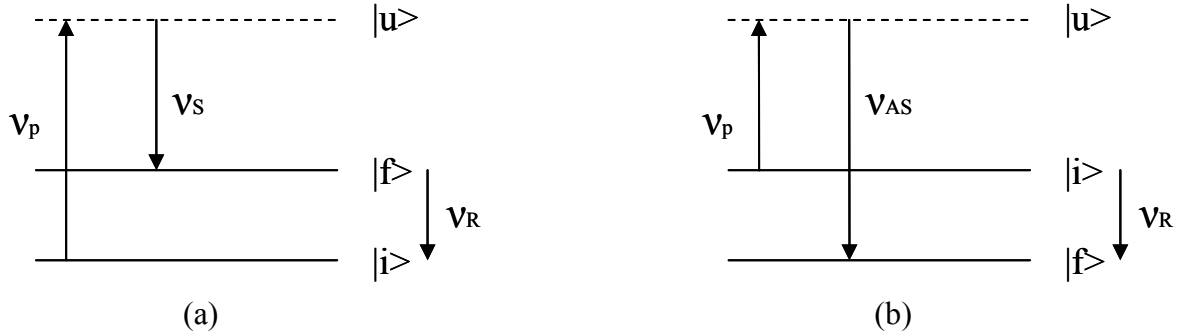
Figure 5.1: Raman process. (a) Stokes light generation and (b) Anti-Stokes light generation.

The aim of studying Raman amplification in barium nitrate (Ba(NO₃)₂) was the investigation of the possibility of pulsed laser operation around 1500 nm. Barium nitrate received special attention because of its unique characteristics. It was recorded that this non-linear crystal has high steady-state SRS gain which is g_R = 11 GW/cm at 1064 nm [29]. Hence, light at the Stokes wavelength sees an amplification factor of $Exp(g_R I_P l_R)$ after a single pass through the Raman medium of length l_R. Here, I_P gives the pump intensity. The Raman shift in barium nitrate is 1048 cm⁻¹ [28]. As described above in equation 5.1, for Stokes Raman scattering, in order to amplify signal at about 1.5 μm which

is the first Stokes components, the wavelength of the pump light has to be around 1.3 μm. This particular wavelength shift can be estimated for our particular design by using equation 5.1.

5.2   Pumping Mechanism

As in the previous KTP OPO study, passively Q-switched Nd:YAG laser was used as the pump source. The pump light near 1.3 μm was used to obtain radiation at 1.5 μm. Operating the Nd:YAG laser near 1.3 μm requires a special set of optics which can prevent the oscillation of the 1064-nm emission.

5.2.1   Pump Energy Calculation for Barium Nitrate (Ba(NO$_3$)$_2$)

Before experimentally studying Raman amplification in Ba(NO$_3$)$_2$, we estimate the minimum pump energy required to obtain Raman oscillation with this crystal. In this section, Raman gain calculations are discussed.

We assumed that the output of the passively Q-switched Nd:YAG laser was focused with a telescope into the Raman crystal. Moreover, Raman laser cavity would be at the same position as the KTP OPO cavity. However, there was a slight difference between the two cavities because the length of the Ba(NO$_3$)$_2$ crystal was 5 cm.

The design of the Raman cavity used in the threshold pump energy calculations is shown in Figure 5.2 below.

M1   C1   M2 (OC)
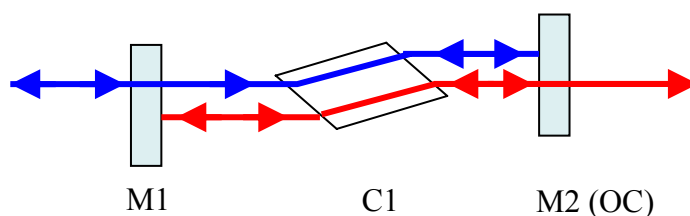
Figure 5.2: The Schematic of the basic Raman cavity.

The first mirror (M1) was highly reflective (R = 98.9%) and the output coupler (M2) was partially reflective (R = 90%) at 1550 nm. The non-linear crystal Ba(NO$_3$)$_2$ (C1) was Brewster cut to minimize reflective losses.

The net differential loss in the cavity accounting for material losses and mirror transmissions is

$$\alpha_T = \alpha_L + \frac{1}{2l_g}\ln(\frac{1}{R_1 R_2}),$$
(5.3)

where α_L is the differential loss coefficient, l_g is the length of the gain medium, R_1 and R_2 are the reflectivities of the first mirror and output coupler, respectively. At threshold, the average differential gain coefficient should equal total loss coefficient hence the differential loss is give by

$$(g_{th})_{average} = \alpha_L + \frac{1}{2l_g}\ln(\frac{1}{R_1 R_2}).$$
(5.4)

We assumed that cavity losses are dominated by mirror transmission loss. Thus, we neglect the first term of equation 5.4. Reflectivities of input mirror and output coupler in our particular Raman cavity design are 1 and 0.9, respectively. The average threshold differential gain satisfies the equation

$$0.9 \times \exp(2(g_{th})_{average} l_g) = 1.$$
(5.5)

For Raman amplification, the differential gain coefficient is given by

$$g_R = g_o \times I_P,$$
(5.6)

where g_o is the Raman gain coefficient which is a characteristics of the non-linear crystal and I_p is the pump intensity. Raman gain coefficient of the barium nitrate crystal for pumping radiation at 1064 nm is reported to be 11 cm/GW [29].

Because the pump intensity varies with position inside the crystal, the overall Raman gain ($g_{average}$) is calculated by integrating over the crystal length according to

$$g_{average} = \frac{1}{l_g} \int_0^{l_g} g_R(z) \times dz \;. \tag{5.7}$$

The power (P) is divided by the area of the beam to determine the intensity of the laser radiation from

$$I_P = \frac{P}{A(z)} , \tag{5.8}$$

where $A(z)$ is the position dependent area of the pump beam. After substituting equations 5.6 and 5.8 into equation 5.6, it can be rewritten as

$$g_{average} = \frac{1}{l_g} \int_0^{l_g} g_o \frac{P}{A(z)} \times dz \;. \tag{5.9}$$

Equation 5.9 was further approximated by replacing the integral with

$$g_{average} \approx g_o \frac{P}{\dfrac{A_1 + A_2}{2}} , \tag{5.10}$$

where A_1 and A_2 are the pump beam areas at the entrance and exit surfaces of the barium nitrate crystal, respectively.

Figure 4.10 shows the variation of the area as a function of position. The barium nitrate crystal is located between the positions of approximately 35 and 40 cm. From the figure, A_1 and A_2 are given by 0.065 cm^2 and 0.2 cm^2, respectively. The average Raman gain was estimated to be

$$g_{average} = 83P \frac{1}{GW} \;. \tag{5.11}$$

When we substituted equation 5.11 in equation 5.5, the power was estimated to be 0.127 MW. By assuming that this is the peak power of the laser, the corresponding pulse energy can be estimated from

$$E = P_{peak} \times t_P,$$ (5.12)

where t_p is the pulsewidth.

At this point, since the 1.3 μm operation of the Nd:YAG laser was not characterized yet, we assumed that the pulsewidth was comparable to that at1064 nm (117 ns). This gives the estimated threshold pump energy of nearly 15 mJ.

5.2.2   Flashlamp pumped 1314-*nm* Nd:YAG Laser

As it was described in the first part, in order to get Raman oscillation near 1.5 μm, Ba(NO$_3$)$_2$ should be excited with photons at around 1.3 μm. For this purpose, a flashlamp pumped Nd:YAG laser was used. However, the strongest laser emission of Nd:YAG lasers occur at 1064 nm [6]. Hence, special mirrors were used to suppress 1064-nm operation and enable the oscillation near 1.3 μm. The configuration and details of the system are illustrated in Figure 5.3.

M1: Plano/Plano, HR at 1340-1350 nm, R<2%@1064 nm.
M2: PR at 8.46% at 1340 nm.
Cham: Flashlamp chamber.
C1: Nd:YAG (6x76mm)%0.9Nd AR at 1064 nm.
L$_T$: 32.5 cm, **L1:** 7.5 cm, **L2:** 17.4 cm.
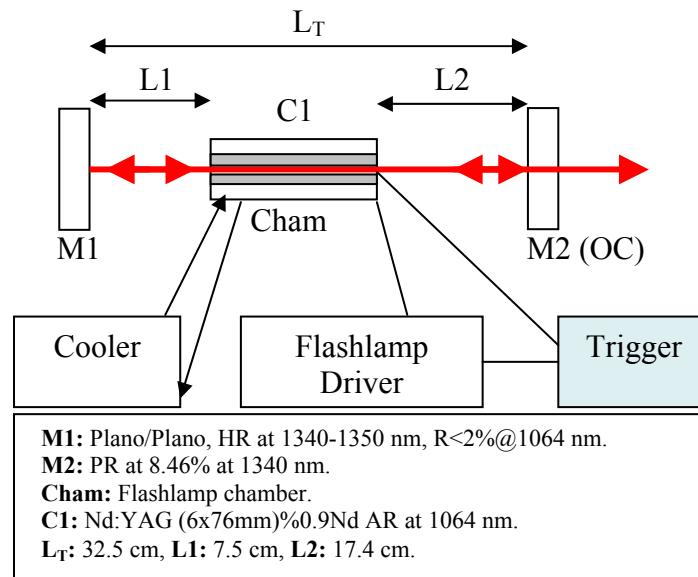
Figure 5.3: The Schematic of the flashlamp pumped 1314-nm Nd:YAG laser.

The efficiency graphs (output energy as a function of input energy and output energy as a function of voltage) of the 1314-nm Nd:YAG laser operating in the long-pulse mode are shown in Figures 5.4 and 5.5. In the first graph, input energies coming from flashlamp were estimated for every voltage value, applied to the flashlamp, by using well known equation 3.1 described in chapter 3 briefly.

$$y = 11.536x - 34.158$$
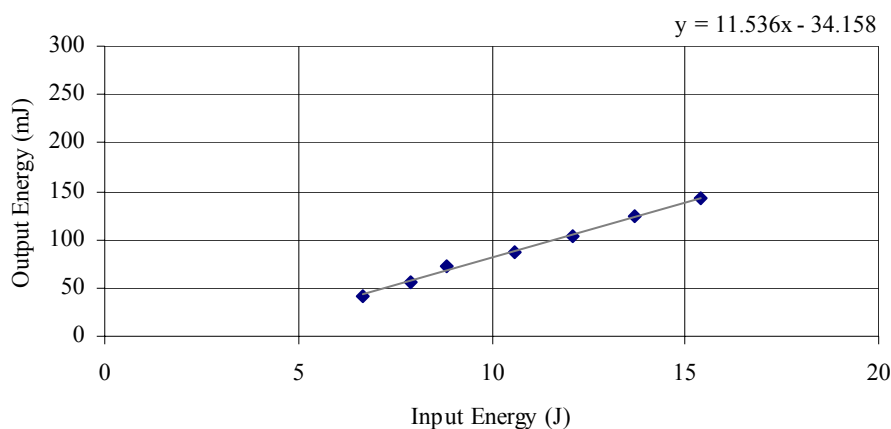
Figure 5.4: Efficiency graph of the 1314-nm Nd:YAG laser showing the output energy as a function of the input energy.
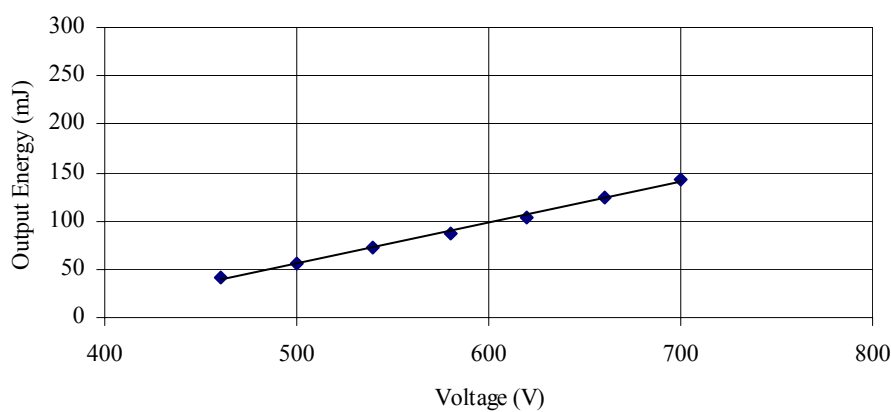
Figure 5.5: Efficiency graph of the 1314-nm Nd:YAG laser showing output energy as a function of the flashlamp voltage.

By using the 8% transitive output coupler and with about 15 J of input electrical energy, about 140 mJ of output energy was obtained at 1314 nm in the long-pulse mode for our particular design. The pulsewidth of the 1314-nm Nd:YAG laser operating in the long-pulse mode was measured to be 250 μs. The pulse profile was recorded with a high-speed InGaAs photodiode and a fast oscilloscope (EZ Digital Oscilloscope DS-1250 250 MHz) with 10 kΩ termination. Figure 5.6 shows the temporal pulse profile of the laser system. The time scale on the horizontal axis is 0.1 ms per division. The output wavelength of Nd:YAG laser was measured with ¼ meter monochromator to be 1314 nm.
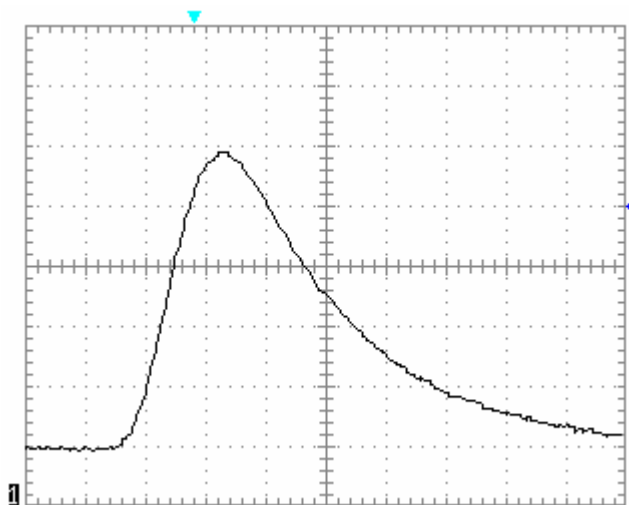
Figure 5.6: The temporal profile of the output pulses from 1314-nm Nd:YAG laser operating in the long pulse mode. The pulsewidth was measured to be 250 μs.

In order to generate very short, high energy optical pulses, passive Q-switching technique was used. In this particular case, we used a Co:MALO crystal as a saturable absorber. It has a small signal transmission of 84% at 1314 nm and it is antireflection coated at 1340 nm. It was positioned at normal incidence inside the laser cavity. Our particular laser design and its details can be seen in Figure 5.7 below.
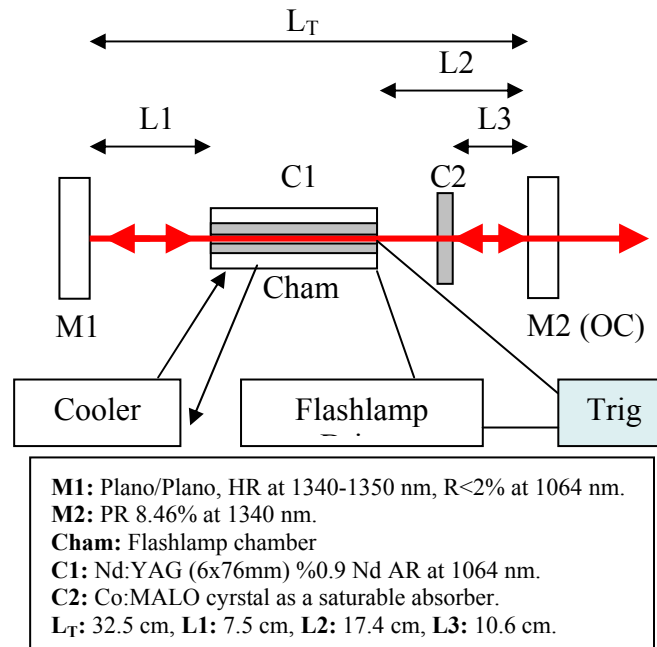
Figure 5.7: The schematic of passively Q-switched Nd:YAG laser at 1314 nm.

During passive Q-switching, the 1314-nm Nd:YAG laser was operated by changing electrical input energy from 8.8 to 13 J with 8% transitive output coupler. The electrical threshold pump energy was obtained to be 8.8 J. Passively Q-switched Nd:YAG laser at 1314 nm generated high energy optical single pulses up to the electrical input energy of 10.2 J. In other words, multiple pulses were generated when the electrical input energy was higher than10.2 J. In Figure 5.8, multiple pulsing is illustrated. The multiple pulse trace was obtained for the 8% transitive output coupler when a voltage of 640 V (electrical input energy = 13 J) was applied to the flashlamp. The total output energy of double pulses was measured to be nearly 25 mJ, corresponding to 12.5 mJ per pulse. The temporal profile was recorded with a high-speed InGaAs photodiode and the pulse was observed on the Tektronix Oscilloscope (TDS-350 200 MHz) with 10 kΩ termination.
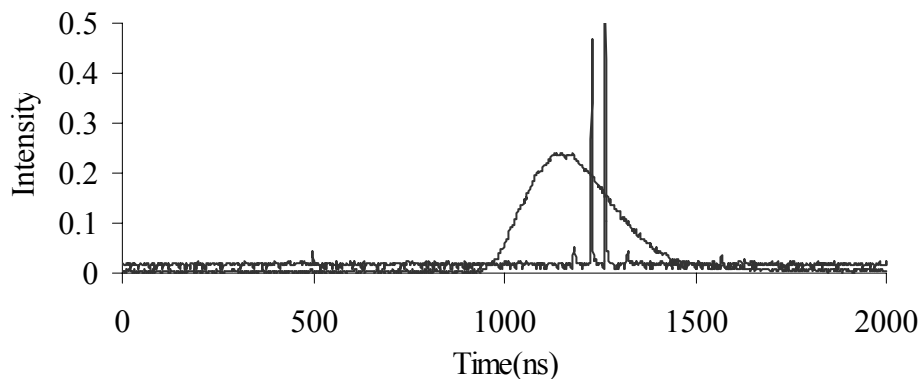
Figure 5.8: Multiple pulsing from the passively Q-switched 1314-nm Nd:YAG laser when the input pump energy was 13 J (output coupler transmission = 8%). The broad pulse preceding the multiple pulse train shows the temporal trace of the flashlamp pulse.

For an input electrical energy of about 10.2 J (applied voltage = 570 V), the highest single output pulse energy of nearly 12 mJ output energy was obtained by using an output coupler with 8% transmission. A single Q-switched pulse is shown in Figure 5.9. A high-speed InGaAs photodiode and Tektronix Oscilloscope (TDS-350 200 MHz) with 10 kΩ termination were used in the recording of the temporal profile of the single Q-switched pulse. The pumping electrical input energy was estimated by assuming a capacitance value of 63 μF in equation 2.11. The pulsewidth was measured to be 140 ns. Figure 5.10 shows the temporal trace of the output pulses from the Nd:YAG laser in Q-switched mode. The pulse profile was recorded with a high-speed InGaAs photodiode and a fast oscilloscope (EZ Digital Oscilloscope DS-1250 250 MHz) with 50 Ω termination.
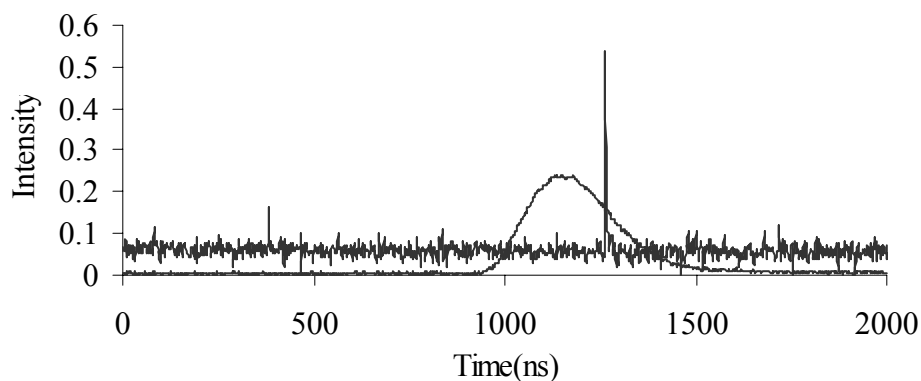
Figure 5.9: Measured temporal trace of the single pulse from 1314-nm Nd:YAG laser operating in the Q-switching mode when the input pump energy was 10.2 J (applied voltage = 570 V). The broad pulse preceding the single pulse shows the temporal trace of the flashlamp pulse.
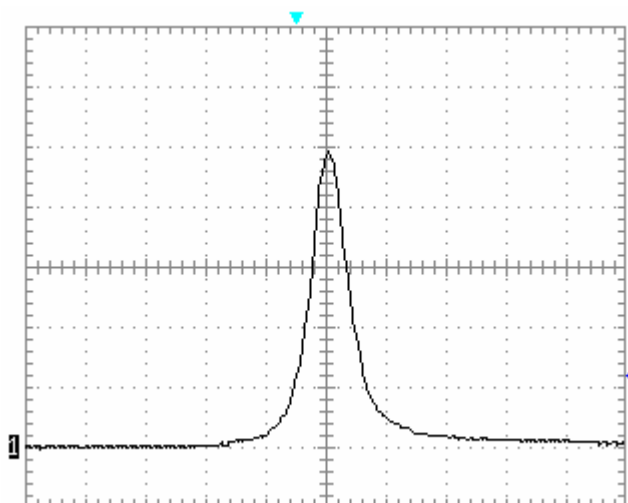
Figure 5.10: The temporal profile of the output pulses from the passively Q-switched Nd:YAG laser with Co:MALO crystal as a saturable absorber. The pulse profile was measured to be 140 ns where the horizontal axis has a calibration of 0.25 μs per division. The output wavelength is 1314 nm.

5.3   Comparison of Experimental Results with Theoretical Results of 1314-nm Nd:YAG laser in Q-switching Mode

As it is discussed in the second chapter, our theoretical modes are based on the analytical derivations and numerical solutions of the rate equations due to the transcendental nature of them. The numerical solutions of rate equation provide information about the system's behavior and performance. In numerical solutions transverse-mode profile of the beam is assumed to be plane-wave. In the Degnan [10] method, only ground-state absorption was taken account. On the other hand, excited-sate absorption was included in the Zhang [11] method.

In this section, comparison of the theoretical estimation of the output pulse parameters (output pulse energy and pulsewidth) with the experimental results of the passively Q-switched 1314-nm Nd:YAG laser is presented. In Table 5.1 below, cavity parameters, gain medium parameters and saturable absorber parameters (Co:MALO) used in models are listed [30, 31].

Cavity Parameters	Symbol	Units	Value
length of the cavity	l_c	cm	32.5
reflectivity of the OC	R		0.08
one way transmission	T_{ow}		0.99
loss	L		0.09

(a)

Er:Glass Parameters	Symbol	Units	Value
emission cross-section	σ_e	cm^2	8.7x10^{-20}
lentgh of the gain medium	l_g	cm	7.6
laser wavelength	λ	nm	1314
effective area	A	cm^2	0.312
induction reduction factor	γ		1.6

(b)

Co:MALO Parameters	Symbol	Units	Value
GSA	σ_{gsa}	cm^2	$2.8\pm0.4\times10^{-19}$
ESA	σ_{esa}	cm^2	$2.0\pm0.6\times10^{-20}$
length of the SA	l_{sa}	cm	0.05
initial transmission	T_0		0.84
induction reduction factor	γ_{SA}		1.3

(c)

Table 5.1: Cavity (a), gain medium (b), and saturable absorber (c) parameters used in the numerical calculations of passively Q-switched 1314-nm Nd:YAG laser with Co:MALO as a saturable absorber.

Numerical calculations demonstrated that the best agreement with experimental results from $L = 9\%$. The experimental results obtained from the passively Q-switched 1314-nm Nd:YAG laser were compared with the theoretical predictions in Table 5.4 below.

Experiment		Theory			
		Degnan		Zhang	
E_o (mJ)	t_p (ns)	E_o (mJ)	t_p (ns)	E_o (mJ)	t_p (ns)
12	140-150	19.3	155.7	15.8	147

Table 5.2: Comparison of experimental and theoretical output energy and pulsewidth of single pulses from 1314-nm Nd:YAG laser operating in the Q-switching mode.

Looking at Table 5.2, the energy and pulsewidth values predicted by the theory are in good agreement with experimentally observed results for the 1314-nm Nd:YAG laser passively Q-switched by the Co:MALO crystal.

5.4   Intra-cavity Raman Laser with Barium Nitrate Raman Crystal

First we tried to obtain stimulated Raman scattering in an extra-cavity pumped configuration. However, because our results were not repeatable, we concentrated on intra-cavity pumping. Two different output couplers, having 90% and 75% reflectivity at 1540-1560 nm were used in this case. By using 90% reflective output coupler, maximum optical pulse energy of 1.5 mJ (0.75 mJ per pulse due to present of two pulses) was obtained at 1524 nm when the applied voltage was 650 V. By using 75% reflective output coupler, maximum optical pulse energy of 1.9 mJ (0.95 mJ per pulse due to present of two pulses) was obtained at 1524 nm when the applied voltage was 640 V. An intra-cavity Raman laser configuration is very simple in principle. The Raman crystal is placed inside the resonator of the pump laser and special optics are used to resonate both the Raman and the pump signals. As a Raman converting medium, Ba(NO$_3$)$_2$ was used. Flashlamp pumped 1314-nm Nd:YAG laser was used as the pump source.

Figure 5.11 shows the details of the intra-cavity pumped barium nitrate Raman laser. The first mirror (M1) was highly reflective (R = 99.8%) at 1340-1350 nm. The radius of the first mirror was 50 cm. The second mirror (M2) was highly reflective (R = 99.8%) at 1550 nm and highly transmitting at 1314 nm. The output coupler (M3) was highly reflective (R = 99.8%) at 1314 nm and partially reflective (R=90%) at 1550 nm. The radius of the output coupler was 50 cm. The length of the intra-cavity Raman resonator was 80 cm. The second mirror (M2) was positioned in the middle of the cavity. The saturable absorber Co:MALO (C2) for Q-switching and Ba(NO$_3$)$_2$ (C3) Raman active crystals were placed as close to the second mirror (M2) as allowed by the mirror holders. This is because the spot size was the smallest near the flat mirror (M2). Energy flow in the intra-cavity Raman laser is as follows. Nd^{3+} ions are first pumped to the upper energy levels by photons emitted from the flashlamp. The optical energy stored in the rod is released in the form of

short nano-second-long pulses at 1314 nm as a result of passive Q-switching. Finally, energy is converted to optical pulses at the first Stokes wavelength of 1524 nm.

M1: Plano/concave, r = 0.5 m, HR at 1340-1350 nm, PR=90% at 1540-1560 nm.
M2: Plano/Plano, HR at 1550 nm.
M3: Plano/concave, r = 0.5m, HR at 1340-1350 nm, PR=90% at 1540-1560 nm.
M3: Plano/concave, r = 0.5m, HR at 1340-1350 nm, PR=75% at 1540-1560 nm.
M4: Plano/plano, HR at 1550 nm, HT at 1340 nm, angle of incidence=45^0.
C1: Nd:YAG (6x76 mm)%0.9Nd AR@1064 nm, **C2:** Co:Spinel crystal as a saturable absorber,
C3: Ba(NO$_3$)$_2$ brewster cut/polished (5x5x50 mm).
Cham: Flashlamp chamber.
L$_T$: 80 cm, **L1:** 18.2 cm, **L2:** 12.8 cm, **L3:** 0.7 cm, **L4:** 0.6 cm, **L5:** 33.7 cm.

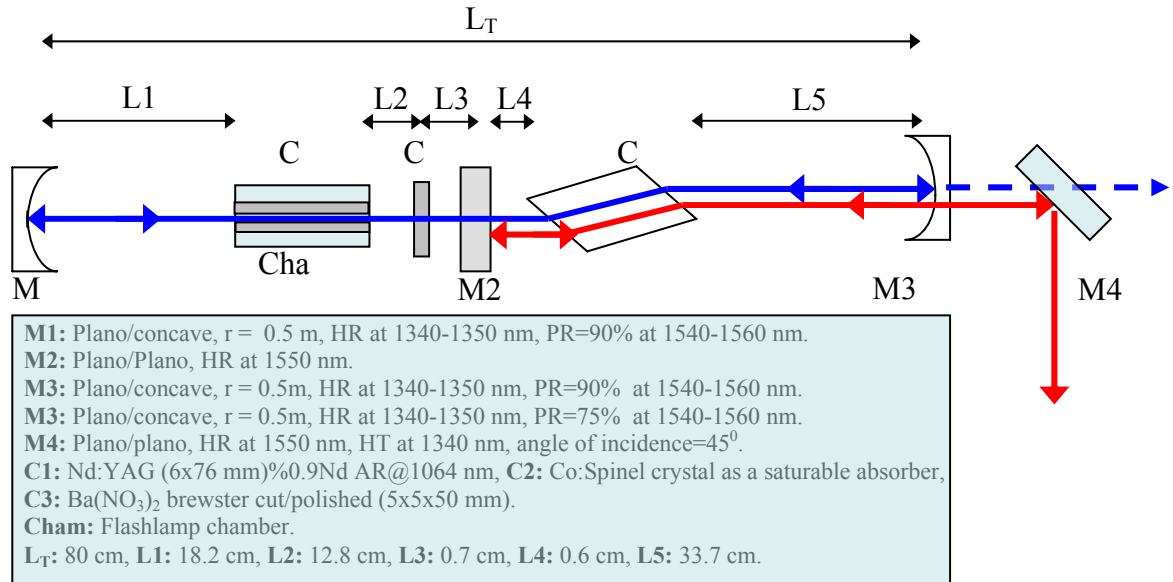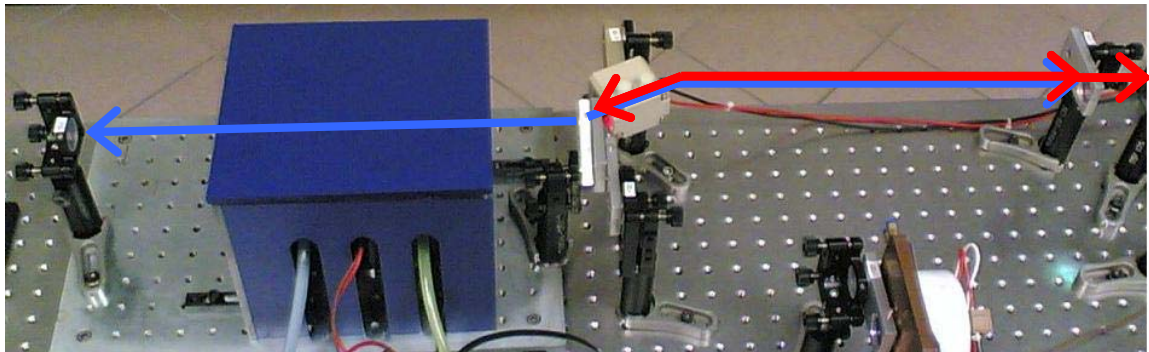Figure 5.11: The Schematic of the Intra-cavity Raman laser.

Figure 5.12: The photograph of the 1314-nm Nd:YAG pumped eye-safe Intra-cavity Raman laser setup.

In this configuration, we used two output couplers having different transmission values at the Raman lasing wavelength. One of them had 10% transmission at 1550 nm and the other output coupler had 25% transmission at 1550 nm. For the first output coupler

(R=90%), average output energy of approximately 0.87 mJ (0.435 mJ per pulse due to present of two pulses) was obtained at 1524 nm when a voltage of 640 V was applied to the flashlamp. By using the 75% reflective output coupler and with same applied voltage across the flashlamp, average output energy of 0.92 mJ (0.46 mJ per pulse due to present of two pulses) was obtained at 1524 nm from our particular intra-cavity Raman laser.

Output pulse energy values for 100 consecutive shots were recorded for both of the output couplers and applied voltage values of 620 V and 640 V. Maximum, minimum and average energy values of the recorded data can be found in Tables 5.3 and 5.4.

Energy performance of the intra-cavity barium nitrate Raman laser at 1524 nm with 90% reflective output coupler. A voltage of 620 V (electrical input energy of 12 mJ) was applied to the flashlamp. Actual energy per pulse is half of the tabulated values due to the presence of double pulses.	
Max. Output Energy:	1.262 mJ
Min. Output Energy:	0.272 mJ
Average:	0.814 mJ
Standard Deviation:	0.252 mJ
Energy performance of the intra-cavity barium nitrate Raman laser at 1524 nm with 90% reflective output coupler. A voltage of 640 V (electrical input energy of 13 mJ) was applied to the flashlamp. Actual energy per pulse is half of the tabulated values due to the presence of double pulses.	
Max. Output Energy:	1.528 mJ
Min. Output Energy:	0.344 mJ
Average:	0.870 mJ
Standard Deviation:	0.309 mJ

Table 5.3: Measured maximum, minimum and average output energies for the barium nitrate Raman laser at 1524 nm with 90% reflective output coupler.

Energy performance of the intra-cavity barium nitrate Raman laser at 1524 nm with 75% reflective output coupler. A voltage of 620 V (electrical input energy of 12 mJ) was applied to the flashlamp. Actual energy per pulse is half of the tabulated values due to the presence of double pulses.	
Max. Output Energy:	1.600 mJ
Min. Output Energy:	0.237 mJ
Average:	0.884 mJ
Standard Deviation:	0.376 mJ
Energy performance of the intra-cavity barium nitrate Raman laser at 1524 nm with 75% reflective output coupler. A voltage of 640 V (electrical input energy of 13 mJ) was applied to the flashlamp. Actual energy per pulse is half of the tabulated values due to the presence of double pulses.	
Max. Output Energy:	1.887 mJ
Min. Output Energy:	0.364 mJ
Average:	0.911 mJ
Standard Deviation:	0.310 mJ

Table 5.4: Measured maximum, minimum and average output energies for the barium nitrate Raman laser at 1524 nm with 75% reflective output coupler.

By using the high-speed detector the output pulsewidth was measured to be 50 ns when the 90% reflecting output coupler was used. Because the stored energy in the atomic medium is released in a fewer number of round trips in the case of the 75% reflective output coupler, the pulsewidth in this case was reduced to 30 ns. The temporal profiles of the Raman pulse are shown in Figures 5.13 and 5.14 for the 90% and 75% reflective output couplers, respectively. The wavelength of the Raman laser was measured with a ¼ meter monochromator to be 1524 nm.
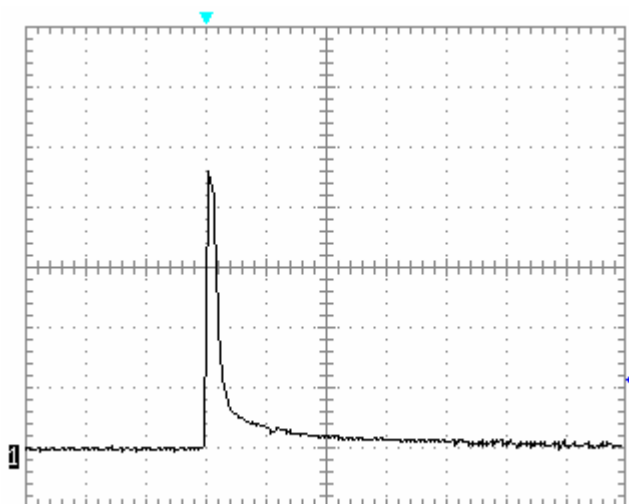
Figure 5.13: Measured temporal profile of barium nitrate Raman laser output pulses at 1524 nm when a 90% reflective output coupler was used. The pulsewidth was measured to be 50 ns.
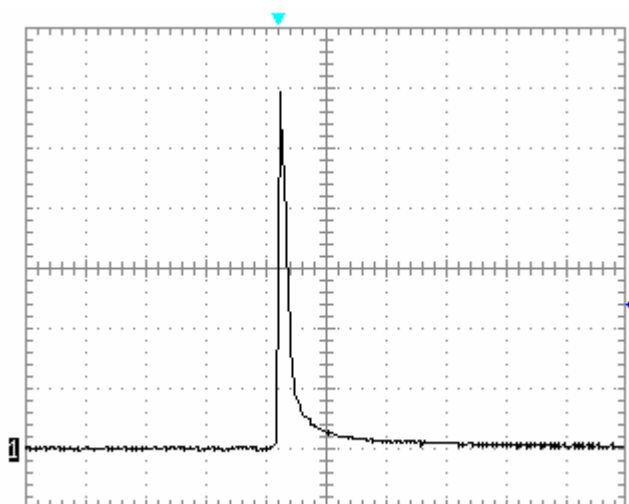
Figure 5.14: Measured temporal profile of barium nitrate Raman laser output pulses at 1524 nm when a 75% reflective output coupler was used. The pulsewidth was measured to be 30 ns.

Overall, use of barium nitrate crystal as a source of eye-safe radiation near 1500 nm has several challenges including the hydroscopic nature of the crystal and the difficulty

involved in aligning a long Brewster cut crystal. We recommend that if such as system is planned for future applications, normal cut and anti-reflection (AR) coated samples should be preferred. Still, an oven operating around 40° Celsius is necessary to prevent the degradation of the crystal surfaces due to ambient humidity.

Chapter 6

PASSIVELY Q-SWITCHED FLASHLAMP PUMPED Er:Glass LASER

6.1   Properties of the Er:Glass Solid-State Laser Material

The erbium doped phosphate glass lasers generate laser output near 1.54 μm in the eye-safe region of the electromagnetic spectrum. Due to the three-level nature of the erbium lasers, they only operate at low temperatures [32] and they have weak absorption of pump radiation [33]. Figure 6.1 gives the details of the three-level system. Initially, all electrons in the atoms of the laser medium are in the ground state. The pump light transfers electrons from the ground state to the level 2 and most of these excited electrons fall down to the intermediate upper laser level by fast and non-radiative decay. Hence, the population in level 2 can be neglected. During the non-radiative decay process, the released energy is transferred to the lattice [13]. Finally, the electrons return to the ground state by the emitting of photons. Pumping intensity should be larger than a threshold value so that population inversion can be established between level 1 and ground state [34].
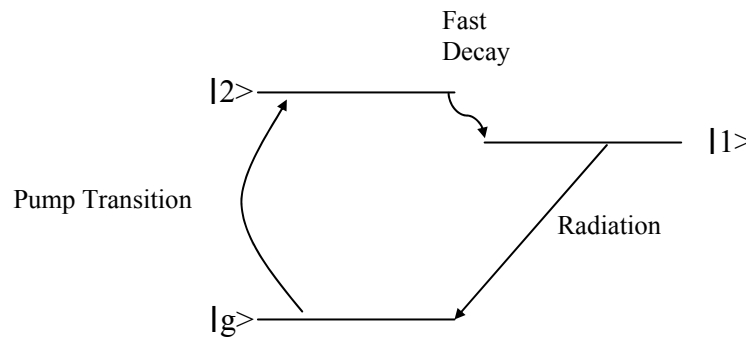
Figure 6.1: Simplified energy level diagram of a three-level laser.

The realization of co-doping with other rare earth ions makes the erbium lasers very attractive systems because co-doping provides satisfactory system efficiency and lasing at room temperature. For instance, erbium can be sensitized with ytterbium (Yb^{3+}). The erbium (Er^{3+}) ions are nearly transparent at about 1 μm [32]. However, pump radiation at 1 μm is absorbed by Yb^{3+} ions [34]. In the co-doped Yb:Er:Glass, radiation from flashlamp at nearly 1 μm excites Yb^{3+} ions from ground state $^2F_{7/2}$ to the upper state $^2F_{5/2}$ [35]. Because of the good matching between states $^2F_{7/2}$ of ytterbium and $^4I_{11/2}$ of erbium, the excited Yb^{3+} ions transfer energy to the upper state of Er^{3+} ([33], [13] and [35]). Then, rapid decay occurs to the upper laser state $^4I_{13/2}$ and lasing is obtained at 1.5 μm as electrons relax down from the upper laser state to the ground level ($^4I_{15/2}$). This energy transfer process in the co-doped Yb:Er:Glass is shown in Figure 6.2 below.

Fast Decay

$^2F_{5/2}$ $^4I_{11/2}$

Energy Transfer $^4I_{13/2}$

Pumping
at 0.9 μm.   Lasing
at 1.5 μm.

$^2F_{7/2}$ $^4I_{15/2}$

Yb^{3+} Er^{3+}
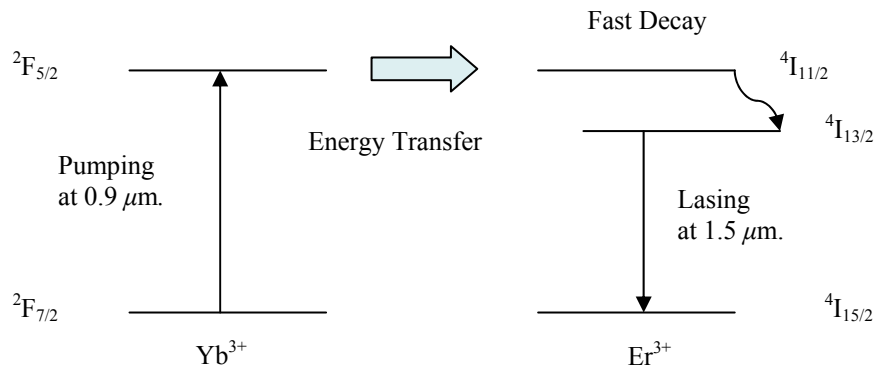
Figure 6.2: The schematic of the energy level in co-doped Yb:Er:Glass.

For flashlamp pumped Er:Glass laser, the absorption efficiency can be improved by doping chromium (Cr^{3+}) in addition to the Yb^{3+} ([33], [13] and [8]). This is because Yb:Er:Glass has a low absorption between 0.4 to 0.9 μm [33]. Cr^{3+} ions are co-doped with Er^{3+} ions in order to increase the excitation efficiency especially in flashlamp pumped systems [36]. Pump radiation coming out from flashlamp at 0.45 and 0.64 μm is absorbed

effectively and photons at 0.76 μm are emitted by Cr^{3+} ions ([33], [13], and [8]). Thus, energy can be transferred from chromium to ytterbium and erbium ions [8]. Figure 6.3 illustrates the energy transfer in the Cr:Yb:Er:Glass crystal.
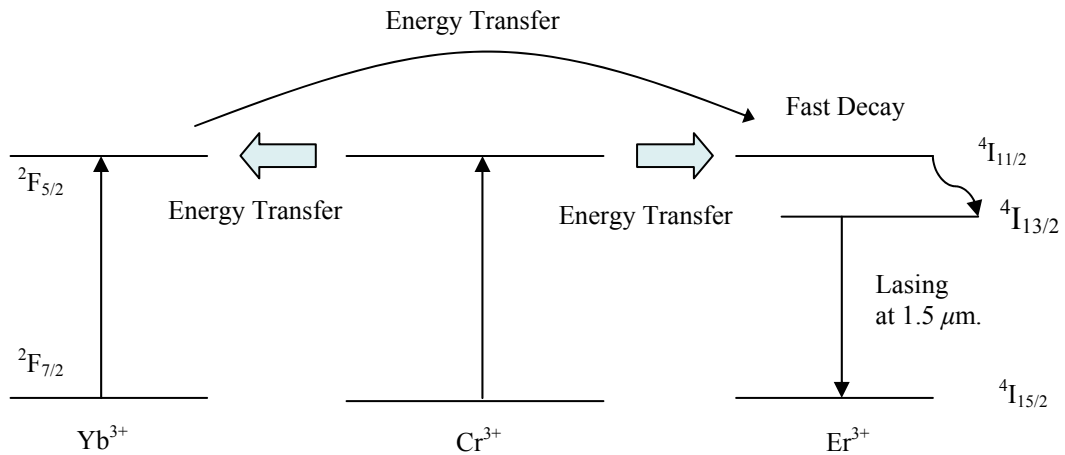
Figure 6.3: The schematic of the energy level in co-doped Cr:Yb:Er:Glass.

6.2   Experimental Setup of Er:Glass Laser

Figure 6.4 shows the schematic of our Er:Glass laser setup. The cavity length of the laser resonator was 17.2 cm. It consists of a flat highly reflective input mirror (M1, R > 99.8% at 1550 nm) and a concave output coupler (r_c = 50 cm). A Xenon flashlamp with 65 mm arc length and 3.7 mm bore diameter was used to pump ø3 x 76 mm Cr:Yb:Er:Glass laser rod. The rod was AR coated at 1535 nm. In addition, the laser rod was kept at room temperature by using water cooling. Two different mirrors with 75 and 90% reflectivity at 1560 nm were employed for output coupling in our Er:Glass configuration. The output wavelength of the Er:Glass laser was measured to be 1520 nm with ¼ meter monochromator.

M1 : plano/plano, HR at 1550 nm.
M2 : Plano/concave, radius 0.5 m, PR=90% at 1540-1560 nm.
M2 : Plano/concave, radius 0.5 m, PR=75% at 1540-1560 nm.
C1 : CrYbEr:Glass (3x76 mm, AR at 1535 nm).
Cham : Flashlamp chamber.
L_T: 17.2 cm, L1: 5.5 cm, L2: 4.1 cm.
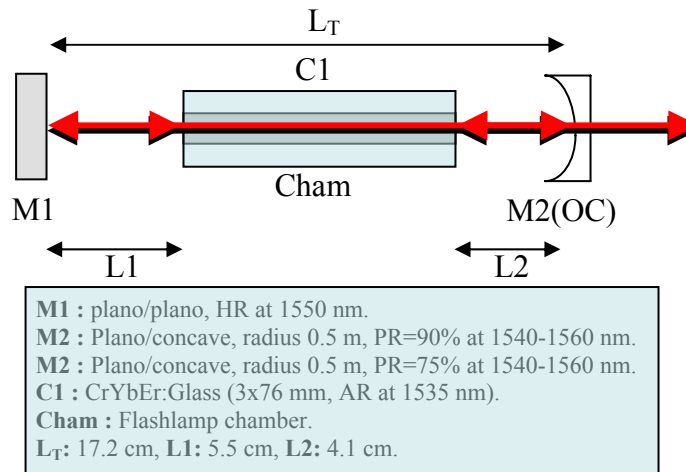
Figure 6.4: The schematic diagram of the flashlamp pumped 1520-nm Er:Glass operating in the long-pulse mode with two output couplers of different reflectivities (75 and 90%) at 1560 nm.

The pulse forming network (PFN) for the flashlamp was designed to generate flashlamp pump pulses of nearly 2 ms duration. The duration of the flashlamp pulses were measured to be 1.8 ms. The pulse profile of the pump pulse was recorded with a high-speed silicon detector and the pulse was observed on the EZ Digital Oscilloscope (DS-1250 250 MHz) with 10 kΩ termination. The temporal pulse profile can be seen in Figure 6.5 (left hand pulse) where the horizontal axis has a calibration of 1 ms per division.
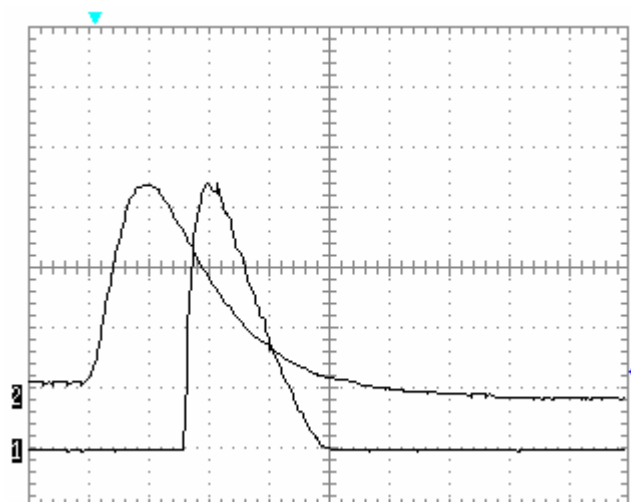
Figure 6.5: The temporal trace of the flashlamp optical pulse and the output pulse of the Er:Glass laser operating in the free running regime. The horizontal axis has a calibration of 1 ms per division.

The Er:Glass laser was passively Q-switched by using a saturable absorber based on Co^{2+}-doped spinel crystal ($Co:MgAl_2O_4$, Co:MALO). The small signal transmission of the Co:MALO crystal was 88% at the lasing wavelength of 1520 nm. The Cr:Yb:Er:Glass laser rod was placed near the concave out coupler and the saturable absorber near the highly reflective flat mirror. A schematic of the passively Q-switched Er:Glass laser with all the relevant components is shown in Figure 6.6.
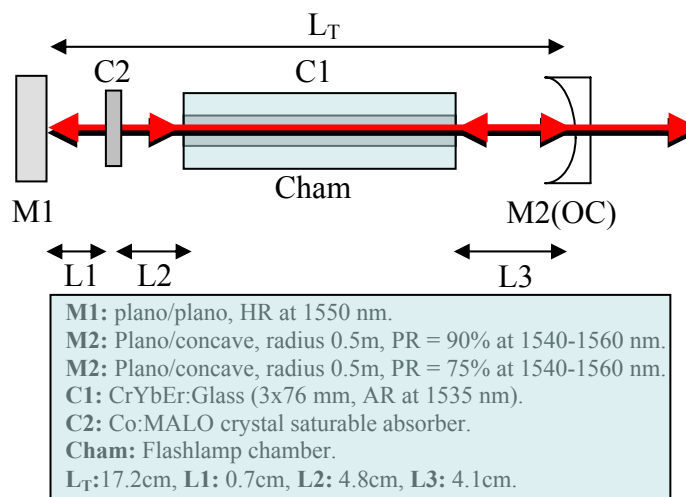
Figure 6.6: The schematic of the flashlamp pumped Er:Glass laser operating in the Q-switch regime with two output couplers of different reflectivities (75 and 90%) at 1520 nm. The Co:MALO crystal was used as a saturable absorber for Q-switching.
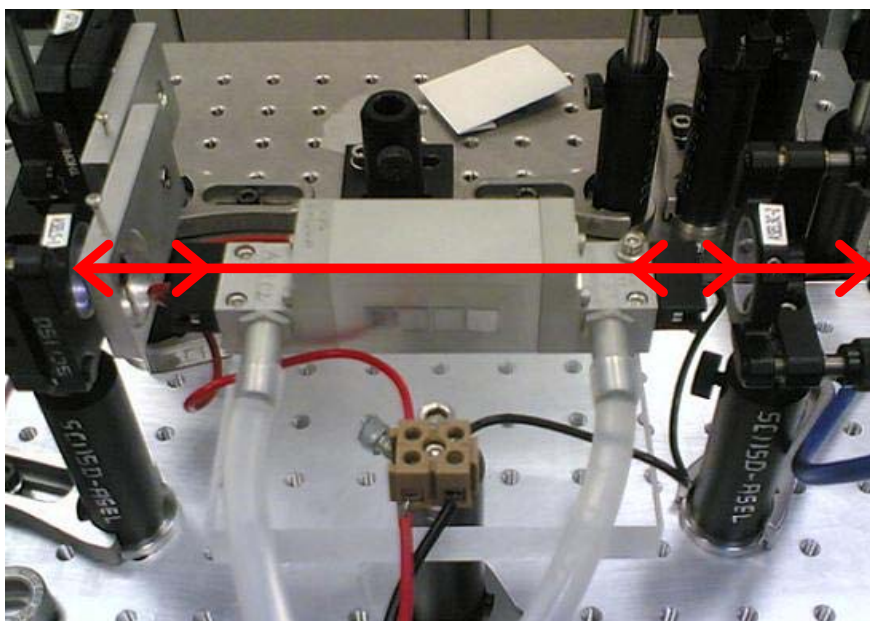
Figure 6.7: The photograph of the flashlamp pumped eye-safe Er:Glass setup.

6.3   Long-Pulse and Q-switched Mode Laser Performance of the Er:Glass

First, the Er:Glass laser was constructed with the 75% reflective output coupler in the long-pulse mode. The schematic of the Er:Glass laser is shown in Figure 6.4. Output pulse energy of about 281 mJ was obtained in the free-running regime when input electrical energy of 82.8 J (applied voltage = 700 V) was applied to the flashlamp. The pulsewidth of the 1520-nm Er:Glass laser was measured to be1.3 ms. Figure 6.5 shows the temporal pulse profile of the laser. The efficiency graphs of the Er:Glass laser operating in the long-pulse mode with 75% output coupler (the output energy as a function of the input energy and applied voltage) are illustrated in Figures 6.8 and 6.9.
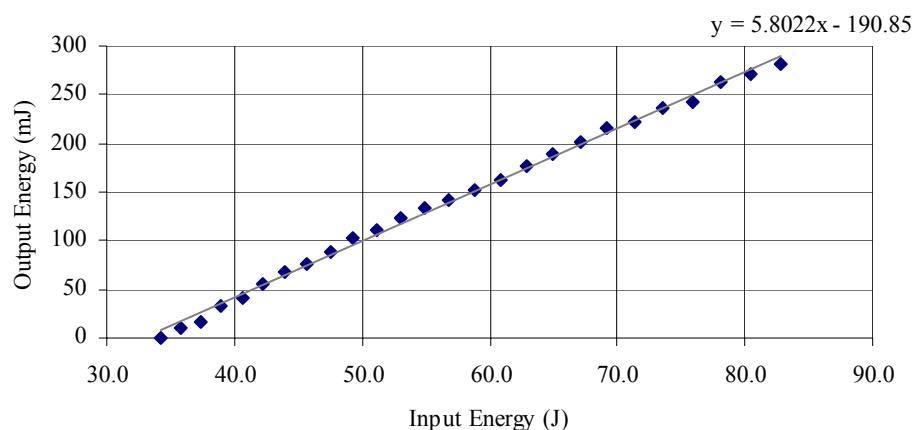
Figure 6.8: Efficiency graph of the Er:Glass laser in the long-pulse mode with the 75% reflecting output coupler showing the output energy as a function the input energy.
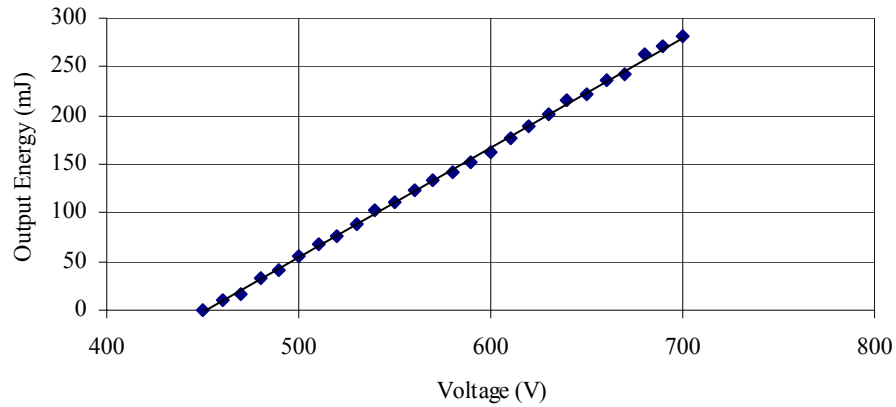
Figure 6.9: Efficiency graph of the Er:Glass laser in the long-pulse mode with the 75% reflecting output coupler showing output energy as a function of the applied voltage.

The Er:Glass laser was operated by changing applied electric energy to the flashlamp from 45 to 69 J (applied voltage from 520 to 640 V) in the Q-switched mode with Co:MALO as a saturable absorber. The electrical threshold pump energy for the Q-switched laser was 45 J. Up to the input pump energy of 51 J (applied voltage = 550 V), the laser generated a single Q-switched output pulse. On the other hand, multiple pulses were obtained when the electrical input energy was above 51 J. The multiple pulse trace was obtained for the 75% reflecting output coupler when a voltage of 640 V (electrical input energy of 69 mJ) was applied to the flashlamp. In Figure 6.10, multiple pulsing is shown. The temporal trace was measured with a high-speed InGaAs photodiode and the pulse was observed on the Tektronix Oscilloscope (TDS-350 200 MHz) with 100 kΩ termination.
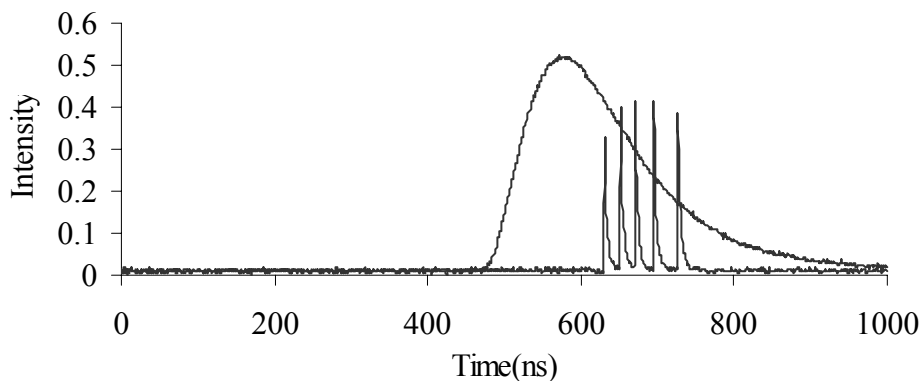
Figure 6.10: Multiple pulsing from the passively Q-switched Er:Glass laser when the input pump energy was 69 J (output coupler reflectivity = 75%). The broad pulse preceding the multiple pulse train shows the temporal trace of the flashlamp pulse.

When the applied voltage was 540 V (electrical input energy of 49 J), the highest single output pulse energy of nearly 21 mJ was obtained by using an output coupler with 75% reflectivity. A single Q-switched pulse is shown in Figure 6.11. A high-speed InGaAs photodiode and Tektronix Oscilloscope (TDS-350 200 MHz) with 100 kΩ termination were used in the recording of the temporal profile of the single Q-switched pulse. The shortest pulsewidth of the Q-switched pulses was obtained to be 40 ns when the cavity length was equal to 17.2 cm. In recording the pulse profiles, a high-speed InGaAs photodiode and a fast oscilloscope (EZ Digital Oscilloscope DS-1250 250 MHz) with 10 kΩ termination were used. The temporal pulse profile can be seen in Figure 6.12 where the horizontal axis has a calibration of 0.25 μs per division.
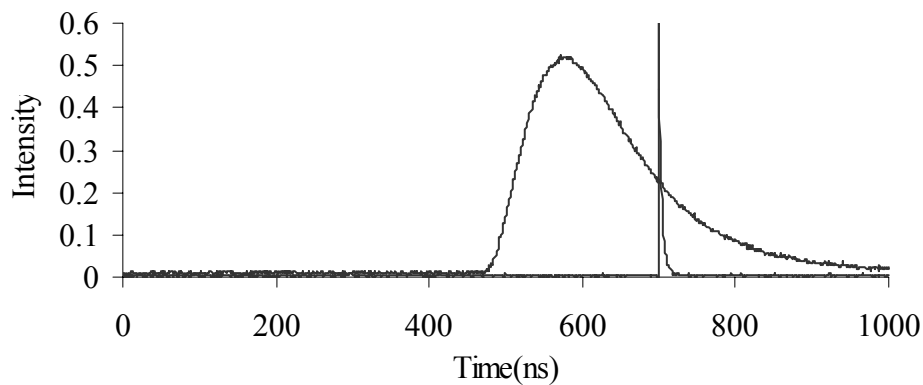
Figure 6.11: Measured single pulse from the passively Q-switched Er:Glass laser when the input pump energy was 49 J (output coupler reflectivity = 75%). The broad pulse preceding the multiple pulse train shows the temporal trace of the flashlamp pulse.
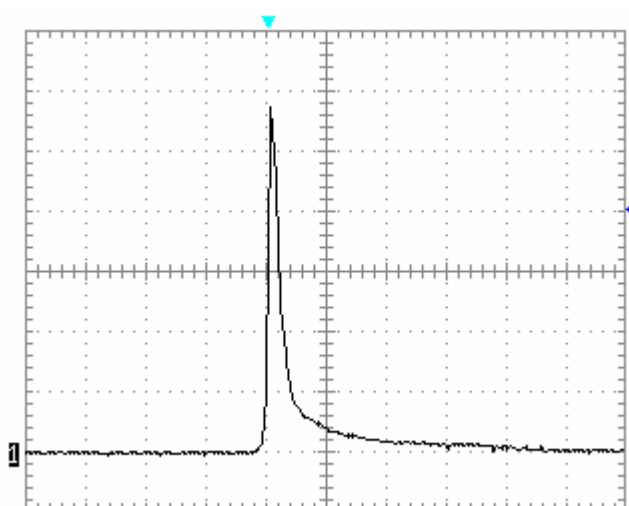
Figure 6.12: The temporal pulse profile of the passively Q-switched Er:Glass laser with 75% reflective output coupler. The pulsewidth was measured to be 40 ns. The horizontal axis was calibrated with 0.25 μs per division.

Second, the Er:Glass laser was constructed with the 90% reflective output coupler in the long-pulse mode. The configuration of the laser is the same as what was described previously. The details of the components and positions in the cavity can be seen in Figure 6.4. In this case, the maximum optical pulse energy of 242 mJ was obtained in long-pulse mode at a pulse repetition rate of 1 Hz, when the applied voltage to the flashlamp was 700V (electrical input energy of 82.8 mJ).

The efficiency graphs of the Er:Glass laser operating in the long-pulse mode with 90% reflective output coupler are illustrated in Figures 6.13 and 6.14. These graphs show the variation of the output energy as a function of the input energy and applied voltage to the flashlamp. In the first efficiency graph, electrical input energies were calculated for every voltage value applied to the flashlamp.
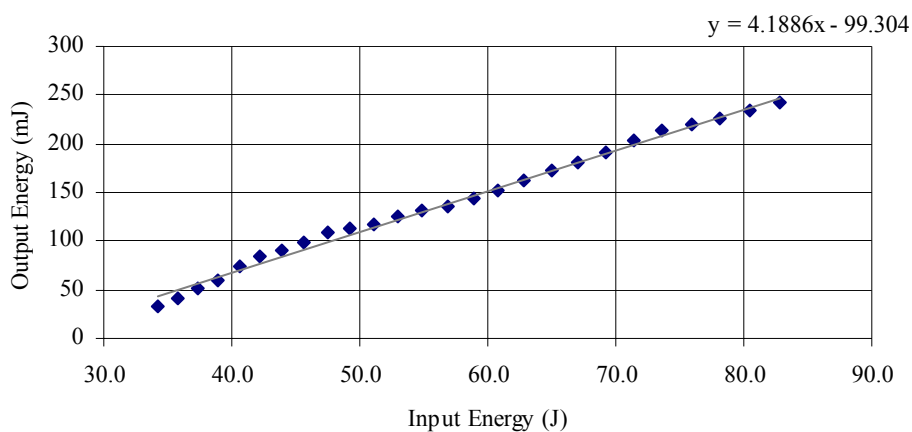
Figure 6.13: Efficiency graph of the Er:Glass laser in the long-pulse mode with the 90% reflecting output coupler showing the output energy as a function of input energy.
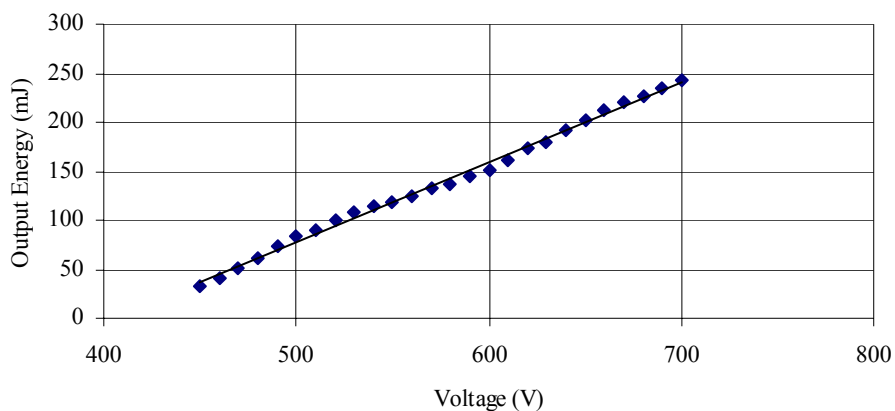
Figure 6.14: Efficiency graph of the Er:Glass laser in the long-pulse mode with the 90% reflecting output coupler showing output energy as a function of the applied voltage.

During passive Q-switching, as high as 13 mJ of output energy was measured per pulse when the estimated electrical input voltage was 47 J (applied voltage = 530 V). The pulsewidth was in the 50-60 ns range. The measured pulse profile of the passively Q-switched Er:Glass laser is illustrated in Figure 6.15.
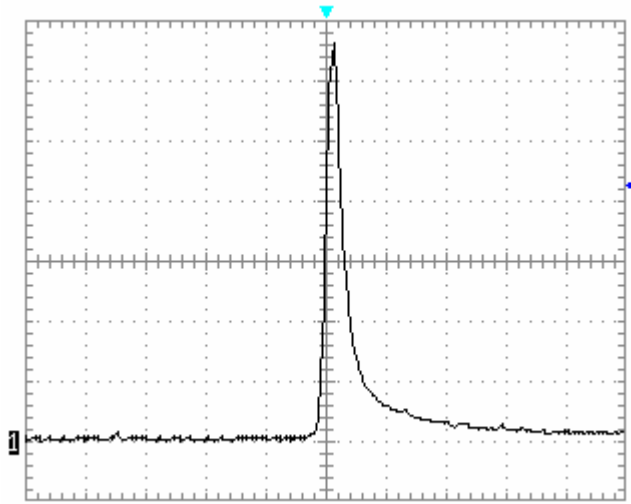
Figure 6.15: Measured temporal profile of the Er:Glass laser operating in the Q-switched mode with 90% reflecting output coupler. The pulse duration was measured to be 50 ns.

Since the stored energy in the atomic medium is released in a fewer number of round trips in the case of the 75% reflective output coupler than in the case of the 90% reflective output coupler, the pulsewidth in this particular configuration was reduced to 40 ns.

6.4   Comparison of Experimental Results with Theoretical Results

In the second chapter, we represented two models of Degnan [6] and Zhang [6] for theoretical analysis of the passively Q-switched lasers. We derived three coupled rate equations describing the mechanism of the passive Q-switching and estimating the key parameters such as output energy, peak power and pulsewidth. Our theoretical models are based on the analytically and numerically solved these differential equations.

In this section of the chapter, the theory predictions of output pulse energy and pulsewidth have been compared with experimental results obtained for the passively Q-switched flashlamp Er:Glass laser. The parameters used for the numerical calculations are listed in Table 6.1 [7, 8, 30, 37].

Cavity Parameters	Symbol	Units	Value
length of the cavity	l_c	cm	17.2
reflectivity of the OC	R		0.75 and 0.94
one way transmission	T_{ow}		0.99
loss	L		0.09

(a)

Er:Glass Parameters	Symbol	Units	Value
emission cross-section	σ_e	cm^2	$8.0 \pm 0.3 \times 10^{-21}$
lentgh of the gain medium	l_g	cm	7.6
laser wavelength	λ	nm	1520
cross-sectional area	A	cm^2	7×10^{-4}
refractive index	n_g		1.54
inversion reduction factor	γ		0.5 - 0.6

(b)

Co:MALO Parameters	Symbol	Units	Value
GSA	σ_{gsa}	cm^2	$2 - 4 \times 10^{-19}$
ESA	σ_{esa}	cm^2	1×10^{-20}
length of the SA	l_{sa}	cm	0.05
refractive index	n_{sa}		1.73
initial transmission	T_0		0.882
inversion reduction factor	γ_{SA}		2.6

(c)

Table 6.1: Names, symbols, units and values of the system parameters used in model.

Numerical calculations demonstrated that the best agreement with experimental results from $L = 9\%$. The results obtained from experimental setup were compared with the theoretical results in Table 6.2 below.

Experiment				Theory			
				Degnan		Zhang	
R (%)	T_0 (%)	E_o (mJ)	t_p (ns)	E_o (mJ)	t_p (ns)	E_o (mJ)	t_p (ns)
75	88	21	40	28.4	38.1	32.8	40.2
94	88	13	50-60	24.1	51.4	21.3	55.1

Table 6.2: Optimal theoretically results and experimentally obtained values of passively Q-switched Er:Glass with Co:MALO saturable absorber.

The experimental and theoretical results showed that minimizing pulsewidth depends on the reflectivity of the output coupler (R) for the fixed initial transmission of the saturable absorber (T_0) and cavity length (l_c). Looking at Table 6.2, experimental results of pulse durations match well with the numerical results. However, there is a worse agreement for output pulse energies. One of the reasons is the experimental error limits. The other reason is the plane wave approximation in the theoretical analysis of the Q-switching. On the other hand, since excited-state absorption in the saturable absorber was taken into account, expected numerical results of Zhang method is much reliable than results of Degnan method.

Chapter 7

CONCLUSIONS

In this study, mainly two methods were investigated for obtaining high-power laser radiation in the 'eye-safe' region. One of them is solid-state lasers with passively Q-switched chromium (Cr), ytterbium (Yb) and erbium (Er) - co-doped Glass laser directly operating at $1.5 - 1.6$ μm. The other method is nonlinear optical conversion of radiation from Nd:YAG lasers. These are Optical Parametric Oscillation (OPO) in KTP crystal and stimulated Raman scattering (SRS) in barium nitrate ($Ba(NO_3)_2$).

With the passively Q-switched Nd:YAG laser pumping the extracavity OPO and by using 90% reflective output coupler, 8.2 mJ pulses with 79 ns duration at 1572 nm were generated. The effective conversion efficiency with respective to the optimized pulse energy from the passively q-switched 1064-*nm* Nd:YAG laser is about 12.2%.

In the intra-cavity Raman configuration, two different output couplers with 75% and 90% reflectivity at 1550 nm were used. When the electrical pumping energy was approximately 13 J, the maximum output pulse energy was obtained to be 1.8 mJ (0.9 mJ per pulse due to presence of two pulses) with 75% reflecting output coupler.

We have described the design and construction of a flashlamp driver for the 1064-nm Nd-YAG, 1314-nm Nd:YAG and 1520-nm Er:Glass lasers operating in the long-pulse mode and passively q-switched regime with a Cr^{4+}:YAG and Co:MALO saturable absorbers. The mechanism of passive Q-switching was further modeled by using a rate equation approach. Overall, experimental results and theoretical calculation of passively Q-

switched 1064-nm Nd-YAG, 1314-nm Nd:YAG and 1520-nm Er:Glass lasers are summarized in Table 7.1.

In Raman laser configuration, in order to maximize the output pulse energy we recommend that normal cut and anti-reflection (AR) coated samples be preferred. Still, the hydroscopic nature of the $Ba(NO_3)_2$ crystal is a problem that limits widespread practical use of this system.

The best results were obtained with the Er-glass laser, where as high as 21-mJ pulses with a duration of 40 ns were obtained at 1520 nm. In this case, the reflectivity of the output coupler was 75 %.

Laser	Wavelength (nm)	Saturable Absorber (SA)	Small-signal Transmission (T_0)	OC Reflectivity (R)	Experimental Results		Theoretical Results			
							Degnan		Zhang	
					E_o (mJ)	t_p (ns)	E_o (mJ)	t_p (ns)	E_o (mJ)	t_p (ns)
Nd:YAG	1064	Cr^{4+}:YAG	0.5	0.54	65-75	117	68.5	99.2	68.7	106.9
Nd:YAG	1314	Co:MALO	0.84	0.08	12	140-150	19.3	155.7	15.8	147
Er:Glass	1520	Co:MALO	0.882	0.75	21	40	28.4	38.1	32.8	40.2
				0.94	13	50-60	24.1	51.4	21.3	55.1

Table 7.1: Parameters, experimental results and theoretical predictions of passively Q-switched 1064-nm Nd:YAG, 1314-nm Nd:YAG and 1563-nm Er:Glass lasers.

VITA

Serhat Tozburun was born in Ankara, Turkey on October 4, 1982. He received his B.Sc. degree in Physics from Middle East Technical University, Ankara, as an Honor Student on June 25, 2005. In August 2005, he was accepted to the Master of Science program in Physics with full scholarship at Koç University, Istanbul, and worked there as a research and teaching assistant until July 2007. His research interests include near-infrared, pulsed solid-state lasers and passive Q-switching. He will continue his Ph.D. work in Optical Science and Engineering program at the University of North Carolina at Charlotte, in the Department of Physics and Optical Sciences.

BIBLIOGRAPY

[1]   Pedrotti, F.L. and L.S. Pedrotti, *Introduction to Optics*. 2nd ed. Vol. 1. 1993, London: Prentice-Hall.

[2]   Xiao, G., M. Bass, and M. Acharekar, *Passively Q-switched Solid-State Lasers with Intra-cavity OPO*. IEEE Journal of Quantum Electronics, 1998. **34**(11).

[3]   Takei, N., S. Suzuki, and F. Kannari, *20-Hz operation of an eye-safe cascade Raman laser with a Ba(NO$_3$)$_2$ crystal*. Applied Physics B, 2002. **74**(6): p. 521-528.

[4]   Jelinkova, H., et al., *Anterior eye tissue transmission for the radiation with the wavelength from the eye-safe region*. Laser Phys. Lett., 2005. **2**(12): p. 603-670.

[5]   Zendzian, W., J.K. Jabczynski, and J. Kwiatkowski, *Intracavity optical parametric oscillator at 1572-nm wavelength pumped by passively Q-switched diode-pumped Nd:YAG laser*. Applied Physics B, 2003. **76**(4): p. 355-359.

[6]   Apanasevich, P.A., et al., *Stimulated Raman conversion of radiation from a Nd:YAG laser with wavelengths of 1.338 and 1.357 um in barium nitrate crystal*. Journal of Applied Spectroscopy (USSR), 2006. **73**(3).

[7]   Kalashnikov, V.L., et al., *Pulse energy optimization of passively Q-switched flash-lamp pumped Er:glass laser*. Applied Physics B, 2002. **75**(1): p. 35-39.

[8]   Bhardwaj, A., et al., *Optimization of passively Q-switched Er:Yb:Cr:phosphate glass laser: theoretical analysis and experimental results*. Appl. Phys. B, 2007. **86**: p. 293-301.

[9]   Murray, J.T., et al., *Generation of 1.5-mu m radiation through intracavity solid-state Raman shifting in Ba(NO3)2 nonlinear crystals*. Optics Letters, 1995. **20**(9): p. 1017-1019.

[10]   Degnan, J.J., *Optimization of Passively Q-Switched Lasers*. IEEE Journal of Quantum Electronics, 1995. **31**(11): p. 1890-1901.

[11]   Zhang, X., et al., *Optimization of Cr4+-Doped Saturable Absorber Q-Switched Lasers*. IEEE Journal of Quantum Electronics, 1997. **33**(12): p. 2286-2294.

[12]   Degnan, J.J., *Theory of the Optimal Coupled Q-switched laser*. IEEE Journal of Quantum Electronics, 1989. **25**(2): p. 214-220.

[13]   Koechner, W., *Solid-State Laser Engineering*. 4 ed. Springer Series in Optical Sciences. Vol. 1. 1996, New York: Springer.

[14]   Kuo, Y.-K., M.-F. Huang, and M. Birnbaum, *Tunable Cr^{4+}:YSO Q-switched Cr:LiCAF laser*. IEEE Journal of Quantum Electronics, 1995. **31**(4): p. 657-663.

[15]   Patel, F.D. and R.J. Beach, *New Formalism for the analysis of passively Q-switched laser systems.* IEEE Journal of Quantum Electronics, 2001. **37**(5): p. 707-715.

[16]   Xiao, G., et al., *Z-scan measurement of the ground and excited state absorption cross sections of Cr^{4+} in Yttrium aluminum garnet.* IEEE Journal of Quantum Electronics, 1999. **35**(7): p. 1086-1091.

[17]   Chen, Y.F., Y.P. Lan, and H.L. Chang, *Analytical Model for Design Criteria of Passively Q-switched lasers.* IEEE Journal of Quantum Electronics, 2001. **37**(3): p. 462-468.

[18]   Sennaroglu, A., *Broadly tunable Cr^{4+} -doped solid-state lasers in the near infrared and visible.* Progress in Quantum Electronics, 2002. **26**: p. 287-352.

[19]   Lipavsky, B., et al., *Some Optical Properties of Cr4+-Doped Crystals.* Optical Materials, 1999. **13**: p. 117-127.

[20]   Shimony, Y., et al., *Repetitive q-switching of a CW Nd:YAG laser using Cr^{4+}:YAG saturable absorbers.* IEEE Journal of Quantum Electronics, 1996. **32**(2): p. 305-310.

[21]   Eilers, H., et al., *Saturation of 1.064 um absorption in $Cr,Ca:Y_3Al_5O_{12}$ crystals.* Applied Physics Letters, 1992. **61**(25): p. 2958-2960.

[22]   Ifflander, R., *Solid-State Lasers for Materials Processing.* 2 ed. Vol. 1. 2001, New York: Springer Series in Optical Sciences.

[23]   Markiewicz, J.P. and J.L. Emmett, *Design of Flashlamp Driving Circuits.* IEEE Journal of Quantum Electronics, 1966. **2**(11): p. 707-711.

[24]   Wegrzyn, J., G. Patonay, and I. Warner, *Versatile Power Supply Circuit for Xenon Flashlamps.* Review of Scientific Instruments, 1988. **60**(1): p. 90-95.

[25]   Wheeler, H.A., *Simple Inductance Formula for Radio Coils.* Proceeding of the IRE, 1928. **16**(10): p. 1398-1400.

[26]   Powell, R.C., *Physics of solid-state laser materials.* Atomic, molecular, and optical physics, ed. G.W.F. Drake. 1998, New York: Springer-Verlag. 1-423.

[27]   HomeWebpage:, *www.coretech.com.cn/english*.

[28]   Pask, H.M., *The design and operation of solid-state Raman lasers.* Progress in Quantum Electronics, 2003. **27**: p. 3-56.

[29]   Cerny, P., et al., *Solid-state lasers with Raman Frequency Conversion.* Progress in Quantum Electronics, 2004. **28**: p. 113-143.

[30]   Konstantinov, V.I., *Saturable absorber Co:MALO crystal for Q-switching of 1.34um NdYAIO3 and 1.54um Er:glass lasers.* Appl. Opt., 1999. **36**(30): p. 6343-6346.

[31]   Huanjun, Q.i., et al., *Co:LMA saturable absorber Q-switch for a 1.319um Nd:YAG laser.* Optics & Laser Technology, 2007. **39**: p. 724-727.

[32]   Tanguy, C. Larat, and J.P. Pocholle, *Modelling of the erbium–ytterbium laser.* Optics Communications, 1998. **153**(1-3): p. 172-183.

[33]   Koechner, W. and M. Bass, *Solid-State Lasers: A Graduate Text*. Springer Series in Optical Sciences. Vol. 1. 2003, New York: Springer.

[34]   Wilson, J. and J.F.B. Howkes, *Lasers: Principles and Applications*. International Series in Optoelectronics. Vol. 1. 1988: Prentice Hall.

[35]   Obaton, A.F., et al., *Excited state absorption in Yb+3 Er+3 - codoped phosphate glasses (ZnO-Al2O3-La2O3-P2-O5) around the I13/2 to I15/2 emission spectral range.* Spectrochimica Acta Part A, 1999. **55**: p. 263-271.

[36]   Mierczyk, Z., et al., *Er3+ and Yb3+ doped active media for 'eye safe' laser systems.* Journal of Alloys and Compounds, 2000. **300**: p. 398-406.

[37]   Scherbitsky, V.G., et al., *Accurate method for the measurement of absorption cross section of solid-state saturable absorbers.* Appl. Phys. B, 2002. **74**: p. 373-374.